

**PONTIFICIA UNIVERSIDAD  
CATÓLICA DEL PERÚ**

**Escuela de Posgrado**



**Performance of muon absorption and scattering methods  
for material discrimination in a portable scintillator-based  
tomographer using CORSIKA and GEANT4 simulations**

Tesis para obtener el grado académico de Doctor en Física que  
presenta:

***Mg. Javier Alonso Rengifo Gonzales***

Asesor:

***Dr. José Luis Bazo Alba***


Lima, 2026

## Informe de Similitud

Yo, José Luis Bazo Alba docente de la Escuela de Posgrado de la Pontificia Universidad Católica del Perú, asesor de la tesis de investigación titulada "Performance of muon absorption and scattering methods for material discrimination in a portable scintillator-based tomographer using CORSIKA and GEANT4 simulations", del autor Javier Alonso Rengifo Gonzales, dejo constancia de lo siguiente:

- El mencionado documento tiene un índice de puntuación de similitud de 28%. Así lo consigna el reporte de similitud emitido por el software *Turnitin* el 30/01/2026. Sin embargo, se tiene que omitir las referencias 1, 2 y 3 (NIM-A, arXiv, PoS) del informe ya que partes de la tesis están publicadas en una revista internacional, también como pre-print y en un proceeding, con autoría del mismo Javier Rengifo. Por tanto, el índice de similitud, omitiendo las referencias señaladas, es de 16%, lo que está dentro del límite establecido.
- He revisado con detalle dicho reporte y la Tesis o Trabajo de Suficiencia Profesional, y no se advierte indicios de plagio.
- Las citas a otros autores y sus respectivas referencias cumplen con las pautas académicas.

Lugar y fecha: Lima, 30/01/2026

Apellidos y nombres del asesor: Bazo Alba, José Luis	
DNI: 41021164	Firma 
ORCID: 0000-0001-9148-9101	

## Acknowledgments

I would like to express my sincere gratitude to all who made this academic journey possible and transformative.

First, my profound appreciation goes to CONCYTEC for the fundamental financial support through the scholarship under Grant 236-2015-FONDECYT. This support was essential for the development of this work.

I thank the PhD in Physics Program of the PUCP (Pontificia Universidad Católica del Perú), and their director Dr. Alberto Gago for cultivate an environment of academic excellence that allowed me to grow as a researcher.

To my advisor, I owe an immense debt of gratitude. Thank you for your invaluable guidance, your infinite patience, and for believing in me even during the most challenging moments of this research. Thanks for the constant support throughout this process.

I also extend my appreciation to Dr. Hernán Asorey and Dr. Mauricio Suárez for their expert advice on the use of CORSIKA and GEANT4, and to Dr. Mauricio Suarez and Dr. Israel Martinez for generously taking the time and suggestions to improve the quality of this work.

To my fellow Master's and Doctoral students, thank you for the camaraderie, stimulating discussions, and shared moments that enriched this journey. I also thank all professors who inspired me with their knowledge and passion for physics.

Finally, and with all my heart, I thank my friends, my family, and my fiancée. Your unconditional love, constant encouragement, and emotional support were the pillars that sustained me. Thank you for understanding my absences, for celebrating my small victories, and for reminding me of what truly matters. This achievement is as much yours as it is mine.

To all of you, my eternal gratitude.

## Abstract

In recent years, muon tomography has appeared as a powerful and innovative technique for non-invasive imaging of both large and small structures, with applications in different fields such as geology, archaeology and security. This study presents the design and simulation of a portable, easy-to-construct detector based on plastic scintillators and silicon photomultipliers using current technology. The system employs a modular approach, where the fundamental detection unit is an  $8 \times 8$  array of plastic scintillator sensors, creating a single detection plane with an active area of  $48.4 \times 48.4 \text{ cm}^2$ . Two such planes are combined to form a sub-detector, enabling the reconstruction of muon trajectories. For full tomographic capability, the complete system uses two of these sub-detectors, positioned on opposite sides of the object under investigation, to measure the scattering angle of muons for material differentiation. The cosmic ray flux reaching Earth's atmosphere was input to CORSIKA to simulate atmospheric muons and other secondary particles at ground level. The geometry and materials of the detector and target object were simulated using GEANT4, which transports the previously generated muon flux. Two muon tomography methods, based on data on muon absorption or scattering, were employed to distinguish objects composed of different materials. Statistical differences were quantified for various object sizes and materials. Using a  $3 \sigma$  threshold in the first method, it was determined that objects made of lead can be distinguished from those made of other materials. The observation times required to differentiate an object made of lead from one made of aluminum were  $1.3 \pm 0.2$  days and  $9.4 \pm 3.7$  days for the first and second methods, respectively.

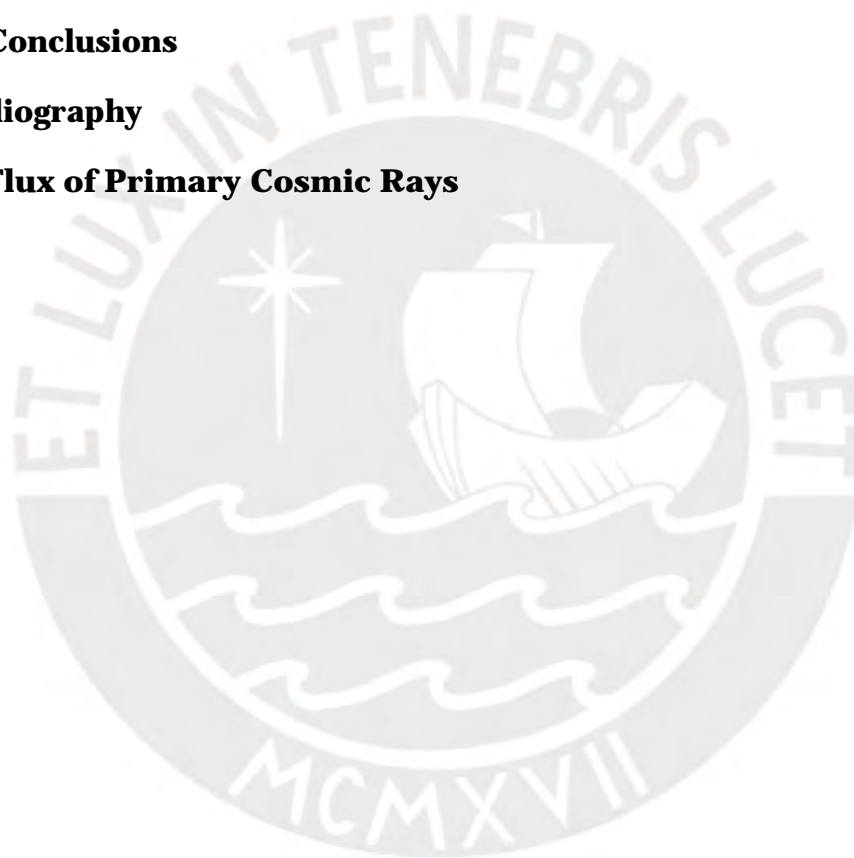
## Resumen

En los últimos años, la tomografía de muones se ha desarrollado como una poderosa e innovadora técnica no invasiva para obtener imágenes de estructuras grandes o pequeñas con aplicaciones en diferentes áreas como geología, arqueología, seguridad y otras. En esta tesis, se presenta el diseño y simulación de un detector transportable y fácil de construir, basado en plásticos centelladores y fotomultiplicadores de silicio de tecnología actual. El sistema emplea una aproximación modular, donde la unidad de detección fundamental es una red  $8 \times 8$  de plásticos centelladores, creando un solo plano de detección con un área activa de  $48.4 \times 48.4 \text{ cm}^2$ . Dos de estos planos forman un sub-detector, habilitando la reconstrucción de la trayectoria de los muones. Para una capacidad completa de la tomografía, el sistema completo usa dos de esos sub-detectores, posicionados en lados opuestos al objeto bajo investigación, para medir el ángulo de dispersión para diferenciar materiales. El flujo de rayos cósmicos que llega a la atmósfera terrestre, fue simulado con CORSIKA y se usó como datos de entrada para los materiales que fueron simulados usando GEANT4, donde el flujo de muones generado previamente fue transportado. Se usaron dos métodos de la tomografía de muones para diferenciar objetos hechos de diferentes materiales: absorción y dispersión. Las diferencias estadísticas para objetos de diversos tamaños y materiales son cuantificadas usando el número de desviaciones estándar. Usando un límite de  $3 \sigma$  en el primer método concluimos que los materiales hechos de plomo pueden ser diferenciados de otros materiales. El tiempo de observación necesario para diferenciar un objeto hecho de plomo de uno de aluminio fue  $1.3 \pm 0.2$  días y  $9.4 \pm 3.7$  días usando el primer y segundo método, respectivamente.

# Contents

<b>1. Introduction</b>	<b>3</b>
<b>2. Cosmic Rays</b>	<b>7</b>
2.1. What are Cosmic Rays? .....	7
2.2. Energy Spectrum.....	7
2.3. Extensive Air Shower.....	9
2.4. Cosmic Rays at ground .....	10
2.4.1. Muons at ground.....	11
<b>3. Extensive Air Shower simulations</b>	<b>12</b>
3.1. Simulation Configuration .....	12
3.2. Extensive Air Shower Results .....	14
<b>4. Muons Through Matter and Tomography</b>	<b>20</b>
4.1. Muon Tomography .....	20
4.2. Muon Angular Distribution .....	21
4.3. Stopping Power.....	21
4.3.1. Energy Loss by Ionization.....	23
4.3.2. Energy Loss by Radiation .....	24
4.4. Muon Tomography Methods .....	26
4.4.1. Absorption .....	26
4.4.2. Multiple Scattering .....	28
<b>5. Muon Detectors</b>	<b>31</b>
5.1. Desktop Muon Detector .....	31
5.1.1. Plastic Scintillators .....	32
5.1.2. Silicon Photomultipliers .....	33
5.2. Nuclear Emulsion Detectors.....	34
5.3. Gaseous Detectors.....	35
5.3.1. Micromegas .....	36
5.3.2. Multi-wire proportional chambers.....	37
5.3.3. Resistive Plate Chambers .....	37
5.3.4. Gas Electron Multiplier (GEM) Detectors .....	38
5.4. Cherenkov Detectors.....	39
5.5. Detector design selection.....	40

<b>6. Detector Design and Simulation</b>	<b>43</b>
6.1. Detector Design and Geometry .....	43
6.2. GEANT4 Simulation .....	47
6.2.1. Detector Definition.....	48
6.2.2. Detector Simulation .....	49
<b>7. Results and Discussion</b>	<b>53</b>
7.1. Simulation Setup.....	53
7.2. Comparative Analysis of Two Muon Tomography Methods for Material Differentiation .....	54
7.2.1. Absorption method .....	56
7.2.2. Scattering Method: Width of the Gaussian Fit to the Scattering Angle .....	59
<b>8. Conclusions</b>	<b>72</b>
<b>Bibliography</b>	<b>74</b>
<b>A. Flux of Primary Cosmic Rays</b>	<b>82</b>



# Chapter 1

## Introduction

Cosmic rays (CR) are messengers of the universe. They travel from different astrophysical objects, arriving at Earth. The information we obtain from them is useful in different research areas such as cosmology, high energy physics, astrophysics, and space weather [1]. At the highest energies, we observe them at the ground with instruments that allow us to detect the products from the particle shower initiated by these CRs after they have interacted with nuclei in the atmosphere. On the other hand, CR in space could affect, because of their energy, electronic circuit components, and the performance of satellites [2].

This work focuses on the most common high-energy charged secondary particle that arrives at Earth's surface: muons ( $\mu$ ), created in the atmosphere after the collision of CR with it. They arrive on the ground despite their short lifetime due to relativistic time dilation granted by their high energy. Muons are created after the decay of charged pions, which are produced high in the atmosphere as follows:

$$\pi^+ \rightarrow \mu^+ + \nu_\mu, \quad (1.1)$$

$$\pi^- \rightarrow \mu^- + \bar{\nu}_\mu \quad (1.2)$$

When these muons transverse matter, they have an interaction that leads to two primary phenomena: attenuation (absorption) due to continuous energy loss and deviation (scattering) from Coulomb interaction with atomic nuclei. By measuring these changes in the muon flux for absorption-based techniques or in the scattering angle for scattering-based techniques, it is possible to infer the density and identify materials within the inspected volume. These properties of muons allow for the reconstruction of the characteristics of the traversed structures [3] by creating 2D or 3D density maps. These methods are called muon tomography and are particularly valuable as an innovative and non-intrusive means to probe vast volumes, from pyramids to volcanoes, that are otherwise inaccessible.

The foundation of muon tomography is the discovery of the muon itself. Carl Anderson and Seth Neddermeyer discovered muons in 1936 at Caltech,

while studying the energy loss of cosmic-ray particles using a thin lead plate [4]. These atmospheric muons are highly penetrating, able to traverse many meters of rock and other dense materials while carrying information about the inner structure of the objects they pass through. Their average energy is approximately 10,000 times that of X-rays [5]. The first application of this property for imaging dates to 1956, when E.P. George used nuclear emulsions to image a tunnel (London Underground) [6]. This was followed around 1960 by the pioneering work of L.W. Alvarez [7], who employed scintillator counters to study the Second Pyramid of Giza in Cairo, Egypt, where he discovered secret passages or hidden chambers. These early experiments open the possibility of developing subsequent investigations such as those of Morishima et al. 2017, who combined nuclear emulsions, plastic scintillators, and gas detectors to examine the interior Khufu Pyramid in Giza [8].

The applications of muon tomography are vast and interdisciplinary. Beyond its roots in particle physics, where muons are used to test and calibrate detectors as in the IceCube experiment at the South Pole [9]. In addition, muons were used to validate their directional reconstruction capabilities by measuring the variation in cosmic rays in the direction of the Moon. The technique is now employed across many fields. These include geology to study the interior structure of volcanoes (e.g, [10], [11], [12]), civil engineering for cavity detection [13], national security for the identification of nuclear materials [14], [15], and nuclear reactor monitoring [16].

Recent progress has focused on improving the detector technology and image reconstruction algorithm. Important developments include a novel image reconstruction algorithm that uses the scattering angle and momentum of muons [17]. There are advances in detector design, such as the portal dual detector setup with plastic scintillating fibers and silicon photomultipliers (MPPC) with 8 milliradians (msr) of angular resolution served in the application of a maximum likelihood expectation maximization method for 3D infrastructure imaging [18], and the high-resolution muon sensor with triangular plastic scintillators and WLS fibers with a spatial resolution of 1.49 mm [19]. Bajou [20] contributed significantly to the data processing algorithm for generating 2D volcanic density maps while evaluating noise interference in track reconstruction. The scope of these technologies continues to expand into areas such as cargo inspection [21], dark matter and environmental sciences [22].

The power of this technique in archaeology is demonstrated by Enrrico (2020), who proposed a novel 3D imaging approach by combining data from three detector positions [23] and more recently by [24], who discovered a hidden chamber in the Hellenistic necropolis of Neapolis, using nuclear emulsion-based detectors. A prominent example in volcanology is the work at Mount Etna by [25], where muon tomography was used to monitor the volcano-tectonic evolution, image the opening of new vents and fractures, and provide data that could predict eruptions in the mid-term.

Atmospheric muons, produced by cosmic rays coming from different parts of the universe, are cost-free and continuously available, making them an ideal resource for research. However, we need detectors to be able to measure the muon tracks and their energy for various applications. For this reason, we explore the most common detector types, such as those using organic plastic scintillators, gaseous media, wires, and photographic films-to design our own portable detector based on CORSIKA+GEANT4 simulations. In this work [26], we determine the optimal geometric parameters of the detector configuration. In addition, we analyze muon absorption and scattering in different materials to distinguish between materials inside larger objects with statistical significance.

Our designed detector is based on plastic scintillators and silicon photo-multipliers (SiPMs). Similar designs have been explored in previous works, such as in [18], which uses plastic scintillating fibers and multi-pixel photon counters (MPPCs), and in [27], which used two scintillator panels. One of the differences between our work and [18] is that their design requires to install the sensor in a heat-insulating box and control the temperature at 17 °C. Additionally, the detector in [27] is not able to reconstruct the track to calculate muon scattering angles, it only measures muon flux. Our work differs from others because we focus on being transportable, easy to build, and capable of material discrimination.

In this study, we investigate muon tomography techniques to differentiate between homogeneous material blocks made of aluminum, lead, iron, concrete, water, or air. To achieve this, we designed a muon track detector with optimized geometrical parameters and simulated a portable mechanical structure with compact dimensions ( 0.48 x 0.48 x 0.2 m<sup>3</sup>).

Our methodology involves a two-step simulation process. First, we used CORSIKA [28] to simulate the atmospheric particle cascade started by cosmic rays. Next, with GEANT4 [29], we modeled the interaction of these secondary particles at the ground level using our detector, which records scintillation photons on the plastic scintillator. To evaluate material differentiation, we analyze two methods: absorption (muon stopping or transmission) and scattering (total deflection angle of Coulomb scattering). We determine which provides the highest statistical significance for material discrimination. An angular resolution of 1° was selected to balance cost and detection efficiency, because a higher resolution would significantly increase detector expenses.

This work is divided as follows: in Chapter 2 we describe cosmic rays, how they interact in the atmosphere to produce a particle shower or extensive air shower, their energy spectrum, features of their flux and muons at ground. Then, in Chapter 3, we explain the CORSIKA software, giving a summary about how it simulates particle cascades at different energies. We simulate protons and nuclei from the CR composition at different energies, to understand how particles are distributed at the Earth's surface. We focus on a realistic simulation considering local and specific parameters such as the

rigidity cut-off point, the type of atmosphere, and the spectrum of the particle flux. In Chapter 4, we describe muon tomography and their physical parameters. For instance, the muon angular distribution, which explains how the muon flux arrives at the Earth's surface, the energy loss when muons travel through materials, and both methods of muon tomography: absorption and scattering. In Chapter 5 we show different types of detectors, including the type that we have used to design ours. In Chapter 6 we present the GEANT4 software and the simulations of mono-energetic muon beams, as well as from the corresponding atmospheric particle spectrum using the cascades resulting from the CORSIKA simulation. In addition, we show the simulation design of the detector, adjusting the geometrical parameters to improve the resolution and the capability to observe muons. In Chapter 7, we describe our results by mentioning the statistical significance for differentiating materials. Finally, in Chapter 8 we give our conclusions, mentioning the challenges and limitations of muon tomography, related to the low flux of atmospheric muons, which could require long acquisition times to generate enough statistics for obtaining high-resolution images.



# Chapter 2

## Cosmic Rays

In this chapter, we explore some characteristics of CR, their showers, their development and interaction in Earth's atmosphere, as well as their energy spectrum and properties at ground level. It is important to note that CR interact with the molecules in Earth's atmosphere and form particle showers that are measured on the ground and will be replicated in this work using CORSIKA. Muons are among the most essential particles in this process because they arrive at the ground in large numbers. These muons are produced by hadronic showers and will be used in this work to examine muon tomography.

### 2.1. What are Cosmic Rays?

CRs are energetic elementary particles, mainly protons and other atomic nuclei (e.g. helium and lithium) [30], which travel to us from different sources, including the Sun, supernova explosions, and unknown origins. CRs move at speeds close to the speed of light and have energies ranging from  $10^{11}$  to  $10^{20}$  eV [31]. These high-energy particles, accelerated at astrophysical sources (called primary cosmic rays), arrive at Earth from isotropic directions. However, they do not reach the ground level because they interact with air molecules in the atmosphere of the Earth [32]. Their interactions produce particle showers (extensive air showers) of new particles called secondary cosmic rays, some of which arrive at the ground.

### 2.2. Energy Spectrum

Primary CRs lose energy during their journey and change direction as a result of galactic and extragalactic magnetic fields, as well as solar wind modulation. For this last reason, there is an anticorrelation between the CR intensity and solar activity [33]. Primary CR can be electrons, protons, helium, carbon, oxygen, iron, and other nuclei (some shown in Fig.2.1). The figure shows the approximate flux of the selected primary CR calculated using a

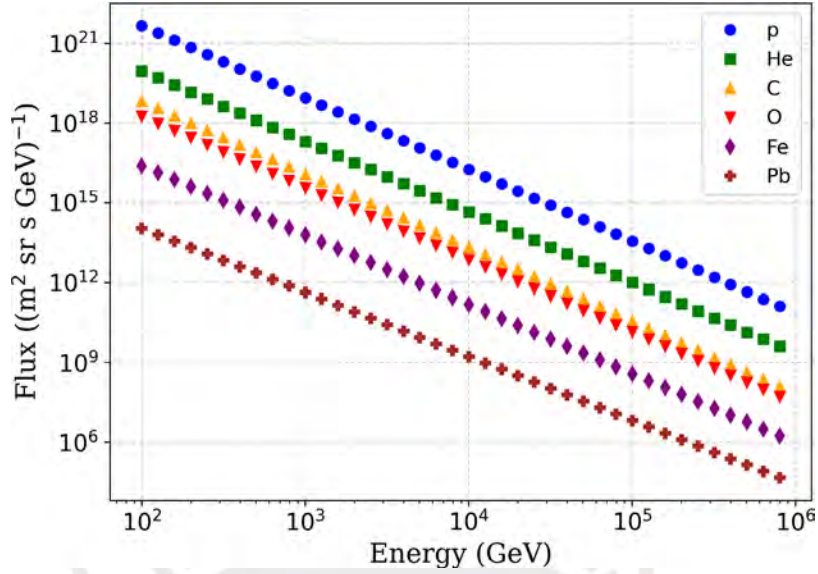


Figure 2.1: Primary cosmic rays nuclei spectra. Notice that the fluxes are down-scaled by constant factors for clarity: He( $\times 10$ ), C( $\times 100$ ), O( $\times 250$ ), Fe( $\times 10^4$ ) and Pb( $\times 10^6$ ). The proton flux is shown without scaling [32].

power law ( $E^\alpha$  with  $\alpha$  ranging from 2.4 to 2.75) in the energy range from  $10^2$  to  $10^6$  GeV with some of these nuclei fluxes down-scaled for better visualization [32].

In addition, Table 2.1 presents the relative abundances of primary CR at 10.6 GeV/nucleon normalized to oxygen [32]. This is an arbitrary normalization based on [34], using abundances from the HEAO-3-C2 experiment. Note that, according to the power law, the spectral indices for each element differ slightly at higher energies. In Section 2.2 we will explain the changes in the indexes at different energies.

Z	Symbol	F	Z	Symbol	F
1	H	750	13–14	Al–Si	0.19
2	He	34	15–16	P–S	0.03
3–5	Li–Be	0.4	17–18	Cl–Ar	0.01
6–8	C–O	2.20	19–20	K–Ca	0.02
9–10	F–Ne	0.3	21–25	Sc–Mn	0.05
11–12	Na–Mg	0.22	26–28	Fe–Ni	0.12

Table 2.1: Relative abundances (F) of cosmic ray nuclei according to their charge (Z) [32].

The energy spectrum of cosmic rays provides important information about their possible origins. This spectrum is usually described by a power law:

$$\frac{dN}{dE} = kE^{-\alpha}, \quad (2.1)$$

where  $E$  is the energy-per-nucleon and  $\alpha \approx 2.7$  is the differential spectral index of the cosmic ray flux and is equal to  $\gamma + 1$ , where  $\gamma$  is the integral spectral index [35].

The spectrum has several features, as shown in Fig. 2.2. First, it decreases dramatically with energy following Eq. 2.1. In the lowest-energy region, the flux is the highest, allowing direct detection of primary CR by balloons or spacecraft. Within the GeV energy range, it is possible to get some information about the effect of solar modulations. Above  $10^5$  GeV, the flux decreases further, requiring detection by an array of detectors on the ground [31]. There are some particular features in the spectrum, such as the *knee* at about  $10^6$  GeV, where the spectral index of the spectrum changes from 2.7 to 3.1. At  $10^8$  GeV another downturn appears, called the *second knee*. Here, the spectral index falls from 3 to 3.3. At this energy, the galactic origin of CR could change to extragalactic, thus presenting the *ankle* at about  $10^9$  GeV. Then, at  $10^{11}$  GeV, the CR flux is extremely low, such as one particle per squared kilometer per century. Finally, another change in the slope of the spectrum is noted, a drastic reduction in the flux. This can be attributed to the *GZK cut-off* (Greisen-Zatsepin-Kuzmin effect) because CR interact with the cosmic microwave background (CMB) and lose their energy during their propagation [36].

### 2.3. Extensive Air Shower

An Extensive Air Shower (EAS) is a cascade of particles produced by transport and interactions between primary cosmic rays and the molecules in the Earth's atmosphere, resulting in secondary cosmic rays. There are two main types of EAS: hadronic and electromagnetic cascades.

The first time that an EAS was observed was in the decade of 1930 by Pierre Auger and colleagues. They detected approximately  $10^6$  relativistic particles at ground level using many detectors spaced up to 300 m apart, inferring that these particles had extremely high energies [38]. Since then, scientists have been developing different ways to detect CR and models to describe EAS such as Heitler's model, describing the development of the electromagnetic cascade, and Heitler, Bethe and Rossi to describe a model for hadronic showers [39]. Modern models incorporate detailed hadronic interactions, such as EPOS, SIBYLL, QGSJET at high energies, and FLUKA or GHEISHA at low energies. These models are briefly described in the CORSIKA guide [40].

Using Heitler's model, we are able to predict important parameters. This model describes the cascade growing exponentially until a maximum number of particles ( $N_{max}$ ) corresponding to a maximum development through the

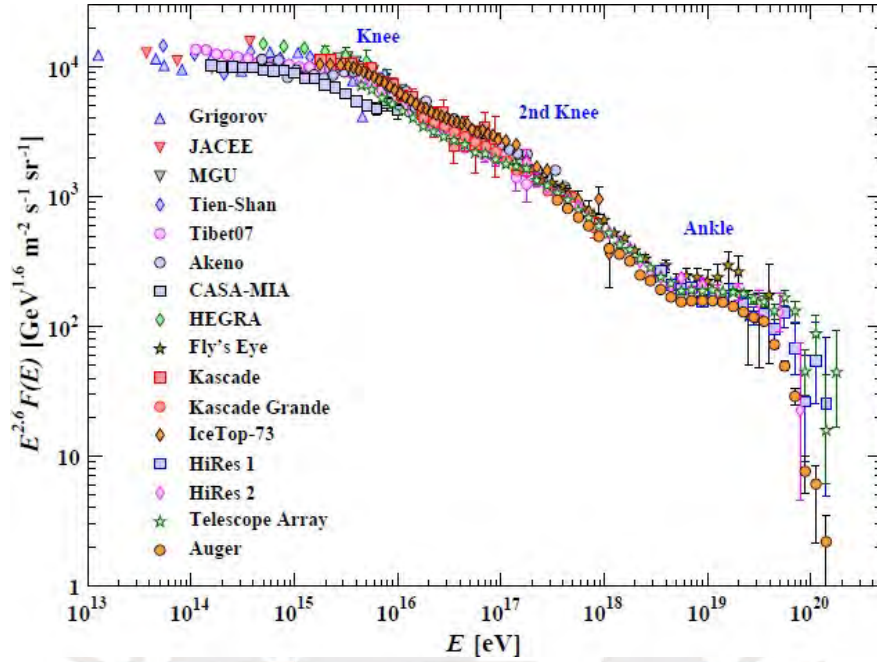


Figure 2.2: All-particle cosmic rays energy spectrum showing main features ("Knee", "second knee" and "ankle") from multiple experiments [37].

atmosphere, called a maximum shower ( $X_{max}$ ). These are important parameters that study the properties of the showers [41]. This model explains how electromagnetic cascades are produced by photons and hadronic cascades are produced by protons and other nuclei. For electromagnetic cascades, photons undergo pair production until a critical energy (85 MeV). However, for hadronic cascades the starting energy of the primary nuclei is divided into two-thirds for charged particles (charged pions) and one-third for neutral particles (neutral pions). Then, they interact with the molecules in the atmosphere until the critical energy of pions (aprox. 25 GeV) [39].

Some particles produced by interactions of primary CR with the terrestrial atmosphere arrive at the surface of Earth. The most produced secondary CR are pions (positive, negative, and neutral). Neutral pions decay into photons, whereas charged pions decay into muons. At the same time, muons decay into electrons and neutrinos.

## 2.4. Cosmic Rays at ground

Primary CR at GeV energies produces enough secondary particles at ground level [42] to reconstruct some properties of the primary particle. Muons, electrons, and photons dominate at the ground level with energies ranging from  $10^{-3}$  to  $10^3$  GeV. Meanwhile, hadrons arrive at the ground in smaller quantities

[43], because most of them interact with nuclei in the atmosphere, producing pions, kaons, and other particles in the EAS, although energetic neutrons can still be detected at ground level [44].

### **2.4.1. Muons at ground**

All muons detected on Earth's surface originate from atmospheric interactions; for this reason, they are called atmospheric muons. When they arrive at ground, they have an average energy of 3-4 GeV and a flux of 167 particles per square meter per second [45]. These muons can penetrate meters of rock, concrete, or other materials because they have enough energy to cross them, although they are slowed and deflected from their trajectory by scattering. The scattering angle (SA) depends on the thickness and composition of the material (i.e. it is Z-dependent (Z: atomic number)) [46], as we will see in Chapter 4.

Muons are the most abundant charged particles at GeV energies [3], [30], [47], as shown in Fig. 3.6. Hadrons e.g., protons, neutrons) arrive in far fewer numbers as mentioned before.

Ground-level muons are very important for studying CR flux, energy spectra, and angular distributions. Their penetrating ability and abundance make them particularly valuable for muon tomography applications. Recent advances have demonstrated the effectiveness of atmospheric muons for non-destructive imaging in various fields, including volcano monitoring [10], nuclear material detection [14], and archaeological investigations of hidden structures [8]. The success of these applications depends on precise measurements of muon scattering angles and flux variation, which will be explored further in Chapters 4.

# Chapter 3

## Extensive Air Shower simulations

CORSIKA (COsmic Ray SIMulation for KAscade) [28] is a program designed to simulate EAS started by CR particles. It was developed for the KASCADE experiment at Karlsruhe, Germany. It is a Monte Carlo code with FORTRAN routines. With CORSIKA, we can study the development and characteristic of EAS in Earth's atmosphere, simulating interactions and decays (where applicable) of nuclei, hadrons, muons, electrons, and photons across an energies range from  $10^{11}$  to  $10^{20}$  eV.

CORSIKA works with many models for high and low energies. The models we used were QGSJET (Quark Gluon String model with JET) and GHEISHA (Gamma Hadron Electron Interaction SHower code) [40], respectively. These models were selected because they incorporate the most recent LHC data. The version of CORSIKA that we used for our simulations was 76900. The program operates through specific input and output files, which we will detail in the following section.

### 3.1. Simulation Configuration

The input file contains all the simulation parameters, which can be modified according to the configuration that we want to simulate. The relevant information for this work was the particle type, number of showers, observation level, energy range, slope of primary energy spectrum, zenith and azimuth ranges, and the Earth's magnetic field.

In this work, we have considered two groups of simulations in CORSIKA with some constant parameters and other variables between the groups. The fixed parameters were geographical:

- Location: Lima, Peru ( $12^{\circ} 2' 35''$  S,  $77^{\circ} 1' 41''$  W).
- Observation altitude: 161 m.a.s.l.

- Magnetic field: 24,8  $\mu\text{T}$  for the vertical component ( $B_z$ ) and -0,4  $\mu\text{T}$  for the horizontal component ( $B_x$ ). Magnetic field information was obtained using the Magnetic Field Calculators [48].
- Angular coverage: Zenith angles from  $0^\circ$  to  $73.8^\circ$  (given the geometrical configuration of the first sub-detector) and azimuth angles from  $-180^\circ$  to  $180^\circ$ .

The first group of simulations is for a general understanding of the distributions of particles on the ground from one thousand showers generated by protons as primary particles with four fixed energies  $10^2$  GeV,  $10^3$  GeV,  $10^4$  GeV and  $10^5$  GeV and one simulation in the range from  $10^2$  to  $10^5$  GeV with energy spectral index 2.7.

We compare the radius of muon distributions at ground produced by primary protons and the muon energy at ground at different primary particle energies in Section 3.2. Also, we show the type of particles that are produced by showers and their distribution on the ground in the energy range from  $10^2$  to  $10^5$  GeV.

The second group of simulations is to introduce the particles produced in the showers as input in the GEANT4 detector simulation with a more realistic energy and type distribution (see Chapter 6) based on plastic scintillator ([49]). The number of showers was calculated as follows:

$$N_{events} = (\text{flux}) \times (\text{area}) \times (\text{time}), \quad (3.1)$$

where  $N_{events}$  is the number of showers. We calculated the atmospheric flux of secondary particles using libraries from the LAGO project [50]. These libraries provided important parameters including spectral indices and nuclear composition of primary cosmic rays, with the nuclear composition modeled according to the framework detailed in the appendix A. In our simulation, we used the incorporated CR flux measurement over a one-hour period, considering the area of the detector that will receive the particles at ground, which was  $48.4 \times 48.4$   $\text{cm}^2$  approximately in an energy range from  $10^2$  to  $10^6$  GeV. The selection of these energy boundaries was motivated by physical considerations. The lower threshold of  $10^2$  GeV was established because primary CRs that arrive in the atmosphere with an energy lower than this interact with the molecules and produce particles that cannot reach the surface. The upper limit of ( $10^6$  GeV) was implemented due to CRs at higher energies than this limit, arrive at the Earth's surface with a very low flux. For low energy, we incorporate a rigidity cutoff of 12.17 GV, as a CORSIKA input parameter, which was extracted from [51]. From the simulation results, we have used the CR flux and obtained the number of showers, which was 23822, for a one-hour observation period.

This approach allowed us to optimize computational efficiency while maintaining physical accuracy in our simulation of atmospheric particle fluxes. The results provide a robust analysis of the extensive characteristics of air showers and their detection parameters.

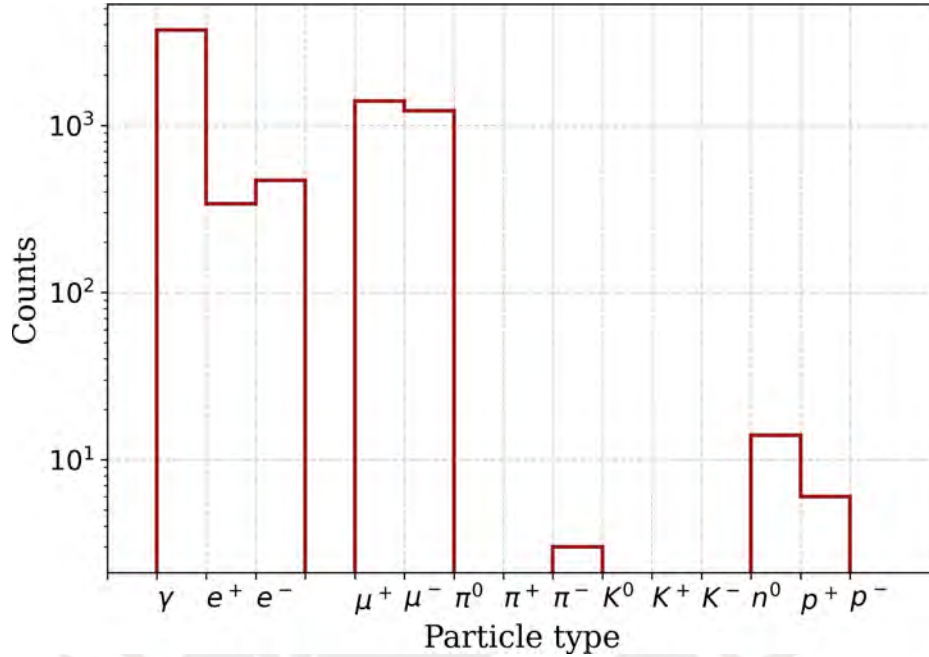


Figure 3.1: Particle distribution at ground generated by 1000 protons in the energy range from  $10^2$  to  $10^6$  GeV. On the X axis label we show the particle type defined in CORSIKA.

### 3.2. Extensive Air Shower Results

The CORSIKA output file contains information about the type of secondary particle, momentum, positions, number of the shower, type of primary particle, and their energies. These data can be extracted in an ASCII file using libraries from [50]. This output will be used as input data for GEANT4 in order to obtain a more realistic modeling of CRs passing through some materials, as we describe in Chapter 6.

From the CORSIKA generated ASCII file, we plot the distribution of the number of particles that reach ground level from the CR flux of the second group of simulations according to their types, as shown in Fig. 3.1, for primary energies ranging from  $10^2$  to  $10^6$  GeV. Apart from gammas, the most abundant, the number of muons are higher than other particles. Charged pions are the result of hadronic interactions in the atmosphere. Since they quickly decay, producing muons, they are hardly observable at ground level. In a similar way and with a much smaller lifetime are kaons, which in general do not reach the ground. Neutrons, protons, and antiprotons can still arrive at the ground, but with a lower number.

In addition, Fig. 3.2 shows the ground-level spatial distribution of particles generated by 1000 primary proton CR with energy ranging from  $10^2$  to  $10^6$  GeV simulated with CORSIKA. The distribution presents the secondary

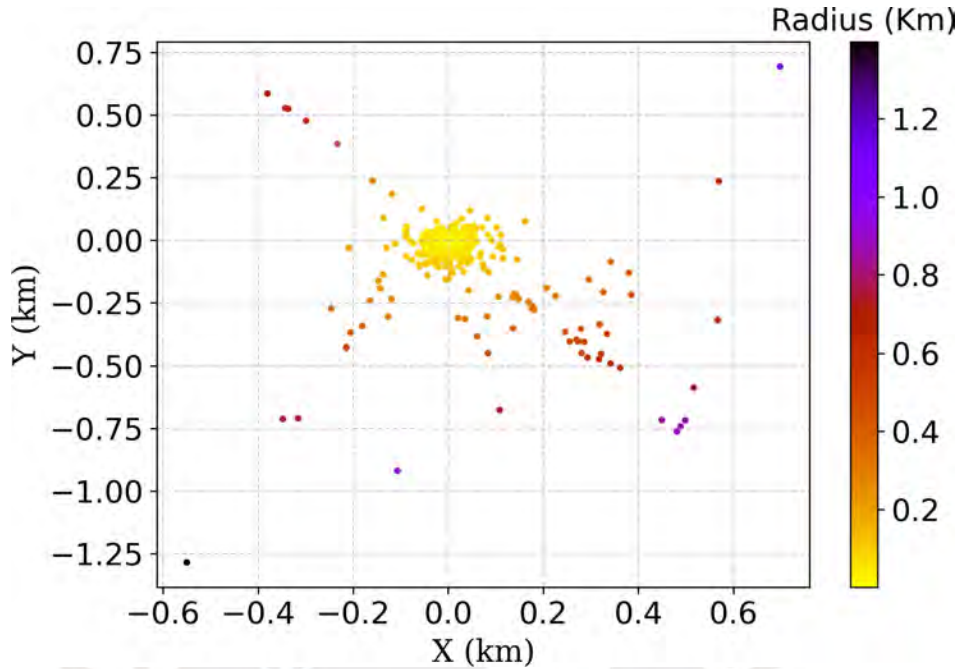


Figure 3.2: Spatial distribution of simulated secondary particles produced by CR with an energy range from  $10^2$  to  $10^6$  GeV in Lima for one minute.

particles concentrate around the core of the shower. Taking this into account, it is possible to calculate a containment radius (which we can see in Table 3.1) that depends on the energy of the primary particle. The importance of this energy-radius relationship provides valuable information about the development dynamics of the shower and the propagation of particles through the atmosphere.

We calculated the number of muons on the ground within a 68% containment radius ( $1\sigma$ ) for various primary energies. Fig. 3.3 shows that all distributions decrease with increasing radius or distance from the center of the shower. Notably, muons produced by higher-energy primary protons propagate significantly farther than those from lower-energy primaries, with the maximum radial extent scaling with primary energy.

The average radial distribution at  $1\sigma$  for muons resulting from primary protons at  $10^2$  GeV is 21.3 m and for  $10^4$  GeV is 10.2 m. This occurs because higher-energy primaries produce secondaries with greater forward momentum, resulting in a narrow collimated shower, while lower-energy primaries produce secondaries with larger emission angles and wider and more diffusive cascade [52]. This fundamental scaling behavior continues to extreme energies, as corroborated by studies of extensive air showers; for instance, Blake et al. in 1995 [53] report that the radial distance of the secondary muons that arrive is 1.2 km for energies ranging from  $10^{15}$  to  $10^{20}$  eV, finding consistent with the shift in the energy distribution maximum to lower energies for muons at larger

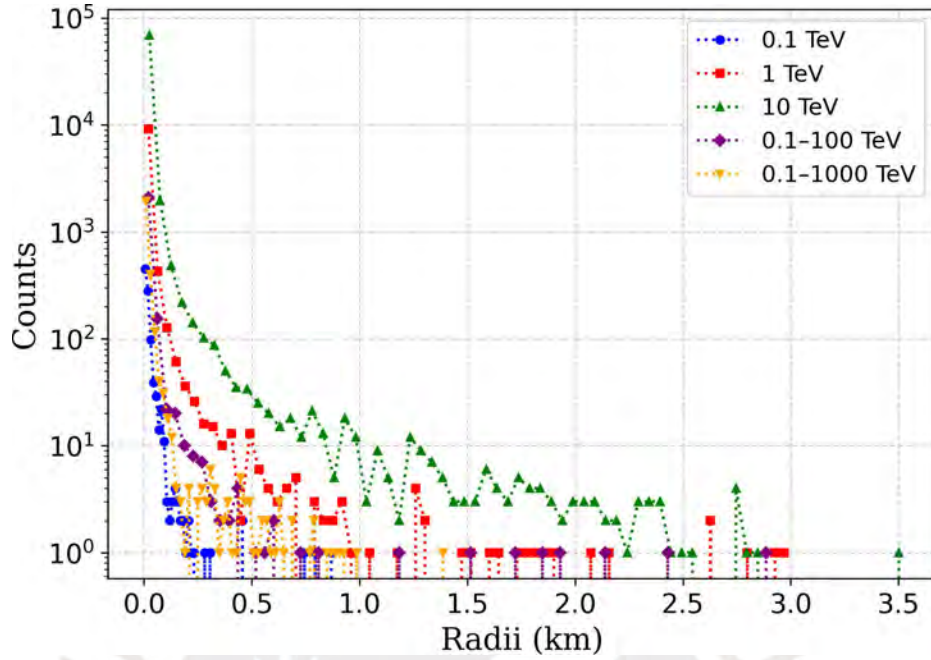


Figure 3.3: Distribution of muon radii at ground produced by primary protons of different fixed energies.

lateral distribution.

Later, we obtained the energy distribution of muons on the ground for different primary energies, which is shown in Fig. 3.4. The mean muon energy resulting from primary protons at  $10^2$  GeV is 6.9 GeV and at  $10^4$  GeV is 30.8 GeV.

We show in Table 3.1 the average values of the number of muons on the ground, their energy, and radius at  $1 \sigma$  of a shower started by primary particles at discrete energies from  $10^2$  to  $10^4$  GeV using a thousand showers and CR nuclei in the energy range simulated for Lima, Peru.

For the second simulation group, we analyze the muon energy distribution considering a realistic flux of primary CR composed of protons, helium nuclei, and heavier elements with energies ranging from  $10^2$  to  $10^6$  GeV—a spectrum representative of the galactic CR that initiate atmospheric particle cascades [54]. Figs. 3.6 and 3.5 show the radii distribution and muon energy distribution for muons, electrons, photons, and other particles, which hit with molecules of the atmosphere for one hour. The secondary muons generated were recorded at ground level by a virtual detector with an effective area of  $0.234 \text{ m}^2$ , which registered 83654 muons over a simulation one-hour period. This corresponds to a muons flux of approximately:

$$\frac{83654 \text{ muons}}{0.243 \text{ m}^2 \times 1 \text{ h}} = 357500 \text{ muons/m}^2/\text{h}, \quad (3.2)$$

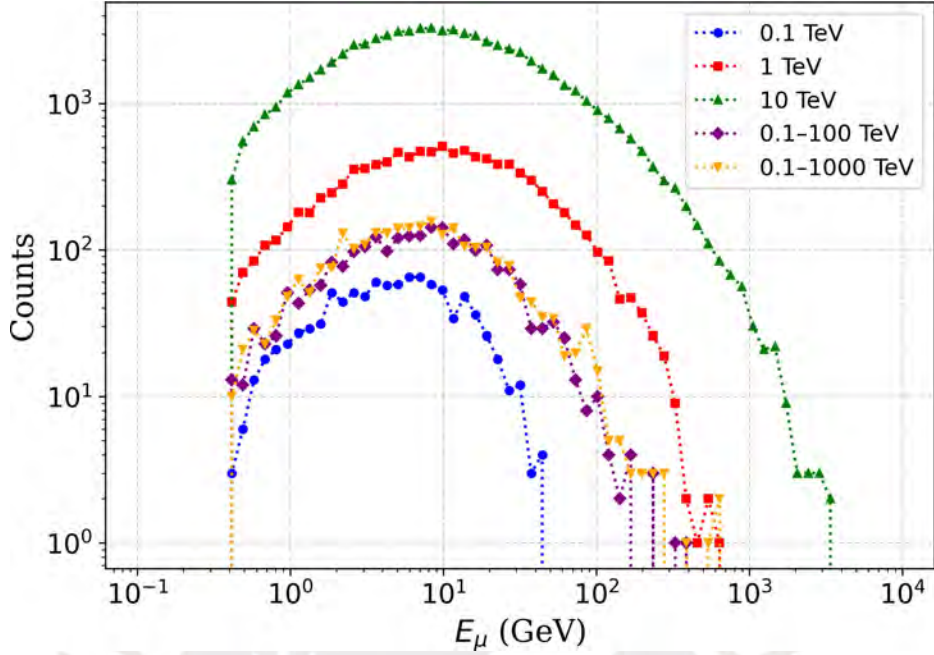


Figure 3.4: Muon energy at ground for different primary particle energies.

which is about 60% of the standard observed muon flux at sea level, typically reported to be around 600000 muons/m<sup>2</sup>/h for energies about a few GeV [55], considering the limited detector area and simulation statistics. Furthermore, the simulated muons had a mean energy of approximately 11.25 GeV, which falls squarely within the well-established experimental energy range for sea-level muons, where the flux peak is typically observed around 2-4 GeV and the mean energy is often reported between 3-4 GeV, extended to high values, for example from 2-30 GeV, depending on the CR primary energy range [31],[54], [55]. The consistency of these results-both in terms of integrated flux and spectral characteristics-with established empirical data validates the accuracy and reliability of the present CORISKA simulation setup in reproducing and propagating secondary muons.

Primary energy	0.1 TeV	1 TeV	10 TeV	0.1 - 1000 TeV
$N_{\mu}$	973	9984	72522	2624
$E_{tot}$ (GeV)	6.9	20.59	30.87	14.33
Radius ( $1\sigma$ ) (m)	21.26	12.77	10.24	16.76

Table 3.1: Average values of the number of particles at ground, total energy and radius at  $1\sigma$  for different primary particles energies.

To evaluate geographical dependencies, we compare three sites: Lima, Peru (12°2'35" S 77°1'41" W), Meyrin, Switzerland - CERN (46°13'42" N

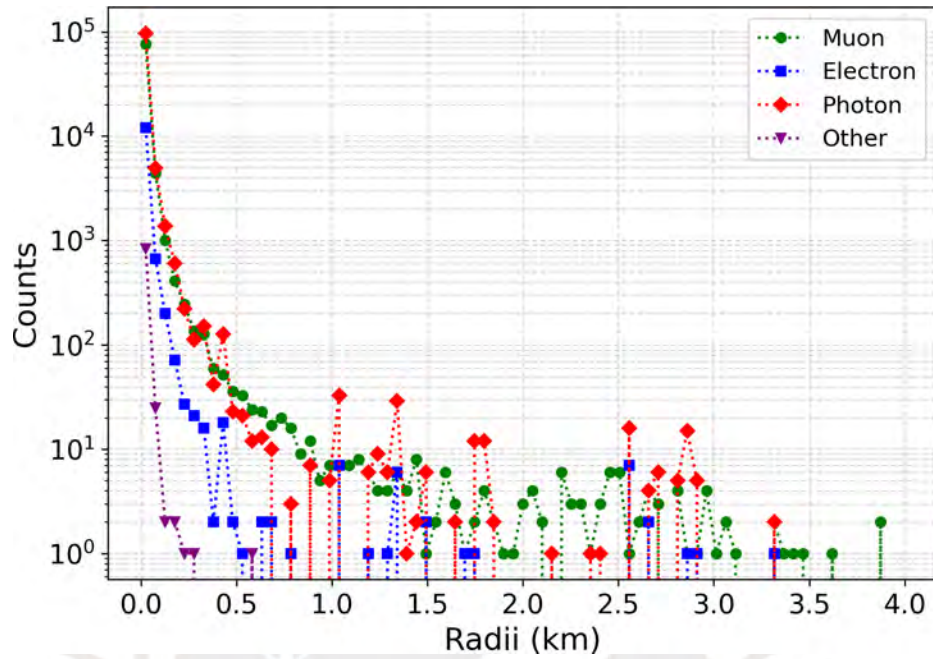


Figure 3.5: Radii distribution of secondary particles at ground from CRs in the range from  $10^2$  to  $10^6$  GeV.

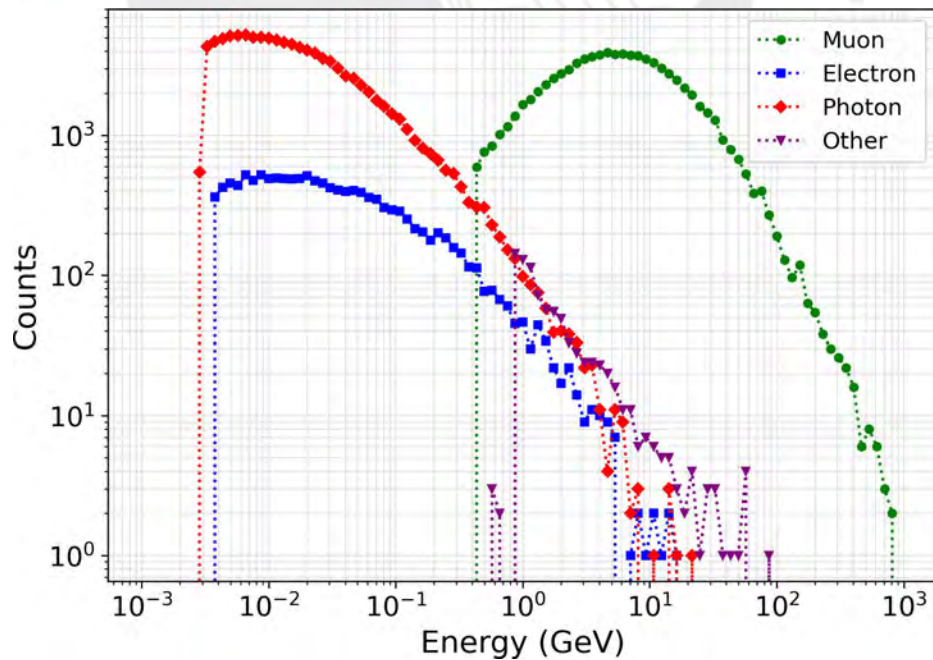


Figure 3.6: Energy distribution of secondary particles at ground from CRs in the range from  $10^2$  to  $10^6$  GeV [26].

6°4 '19 " E) and Achorage, Alaska (64°48 '29 " N 151°0 '14 " W). In Table 3.2 we show the characteristics of each site: altitude, components of the magnetic field ( $B_x$  and  $B_z$  for October 21, of 2020) and the rigidity. This characteristic can change the result of the CR showers. In Table 3.3 we present the parameters explained before (radius at 68%, muon energy distributions, and the number of muons on the ground) for each site.

Sites	Lima, Peru	Meyrin, Switzerland (CERN)	Achorage, Alaska
Altitude (m)	120	446	31
Rigidity (GV)	12.34	4.63	1
$B_x$ ( $\mu\text{T}$ )	24.8	22.2	12.5
$B_z$ ( $\mu\text{T}$ )	-0.41	42.1	54.8

Table 3.2: Characteristics of the simulated sites of CRs showers in a range from  $10^2$  to  $10^6$  GeV. For this comparison we simulated 1000 showers.

Sites	Radius [km]	Energy [GeV]	part/cm <sup>2</sup> min
Lima	1.35	4.43	0.99
Meyrin	1.61	4.63	0.81
Achorage	1.53	4.57	0.86

Table 3.3: Average values of the number of particles at ground, mean total energy and radius at  $1\sigma$  for different sites.

The maximum variation of the flux is on the order of 20%, where Lima was the site with the highest particle flux. Also, we can see that the radius for Lima is 0.36 km less than that of Meyrin and 0.18 km less than that of Achorage, and the energy for Lima is 0.2 GeV less than that of Meyrin and 0.14 GeV less than Achorage. The variation correlates with Lima at the minimal horizontal magnetic field, Meyrin at a higher altitude than other sites, and the rigidity cutoff varying with sites affecting low-energy showers.

# Chapter 4

## Muons Through Matter and Tomography

This chapter explains the physics behind muons that arrive at ground level and their propagation through matter, which form the basis for different muon tomography techniques.

### 4.1. Muon Tomography

Muon tomography is an application of the measurement of atmospheric muons to reconstruct structural information. These muons arrive from different directions to the surface after having interacted with molecules in the atmosphere. When muons arrive at ground, they have a known angular distribution, which we will describe in Sec. 4.2. Muons lose their energy through different physical mechanisms when they pass through different materials until they stop, losing all their energy, as explained in Sec. 4.3. As a result, muons that interact with different objects will change their original direction. Given these two phenomena, absorption by the material and dispersion (that is, scattering from their original direction), two methods to identify with which material muons are interacting will be presented in subsection 4.4.

The interaction of CR with the atmosphere molecules produces a cascade of secondary particles, among which muons constitute the most abundant and energetic of these particles capable of reaching the surface of the Earth and can be easily measured. These particles exhibit a characteristic average energy of 3 to 4 GeV and a sea level flux of  $167 \text{ particles m}^{-2}\text{s}^{-1}$  [45]. At these energies, muons can have exceptional penetrating power through dense material such as rock and concrete. The interaction of muons with matter is shown through two measurable effects: gradual energy loss (attenuation) and directional changes (scattering). These fundamental physical processes support muon tomography techniques [56], allowing the non-destructive examination of structural features, which will be elaborated in subsequent sections.

## 4.2. Muon Angular Distribution

Most muons are produced at a height of around 15 km in the atmosphere of Earth [32]. At low energies and from a horizontal direction, the muon intensity is reduced because muons interact with molecules in the atmosphere and do not arrive at the Earth's surface. However, the intensity increases at high energies because the parent muons can travel longer distances [47].

Muons arrive at ground in a specific angular distribution. This distribution is proportional to  $\cos^2\theta$ , where  $\theta$  is the zenith angle for mean muon energies of 3 GeV [32]. Muons fade fairly with an increasing zenith angle. Also, at high energies (approximately 1 TeV) the angular distribution follows the dependence  $1/\cos(\theta)$  [47]. However, the muon flux generated for particles with energies higher than  $10^5$  GeV decreases. For this reason, the proportional distribution to  $\cos^2\theta$  is the most important for this work.

The muon flux as a function of energy  $E$  and zenith angle  $\theta$  can be written as [57]:

$$I(E, \theta) = I_0 N (E_0 + E)^{-n} \left(1 + \frac{E}{\eta}\right)^{-1} D(\theta)^{-(n-1)}, \quad (4.1)$$

where  $I_0$  is the vertical muon flux integrated over energy,  $N$  is the normalization constant,  $E_0$  is the additional energy loss due to hadronic and electromagnetic interactions with air molecules, the parameter  $\eta$  changes the power in the high-energy part and  $D(\theta)$  is an expression of column density for muon trajectory inclined in the curved atmosphere of Earth, which depends on the distance to the point in the atmosphere where the muons enter, the vertical or zenith distance, and  $\cos^{n-1}\theta$ .  $n$  is the power index of the energy spectrum. If  $n = 3$ , then this gives the distribution  $\cos^2\theta$ , which describes the angular distribution of the zenith.

According to the distribution, the muon flux decreases when the zenith angle increases because muons have to travel longer distances before they reach the ground or the detector, as shown in Fig. 4.1, in which the muon distribution is compared with the distribution  $\cos^2\theta$ . This means that if we want to observe an object horizontally, a longer exposure time is necessary [15].

## 4.3. Stopping Power

Muons pass through matter interacting and losing energy by ionization and radiation [58], before they decay or have an inelastic collision. The energy loss or stopping power is represented as follows:

$$-\frac{dE}{dX}, \quad (4.2)$$

where  $E$  is the kinetic energy of the charged particle, expressed in eV and  $X$  is the distance or range that the particle can travel within the density of the

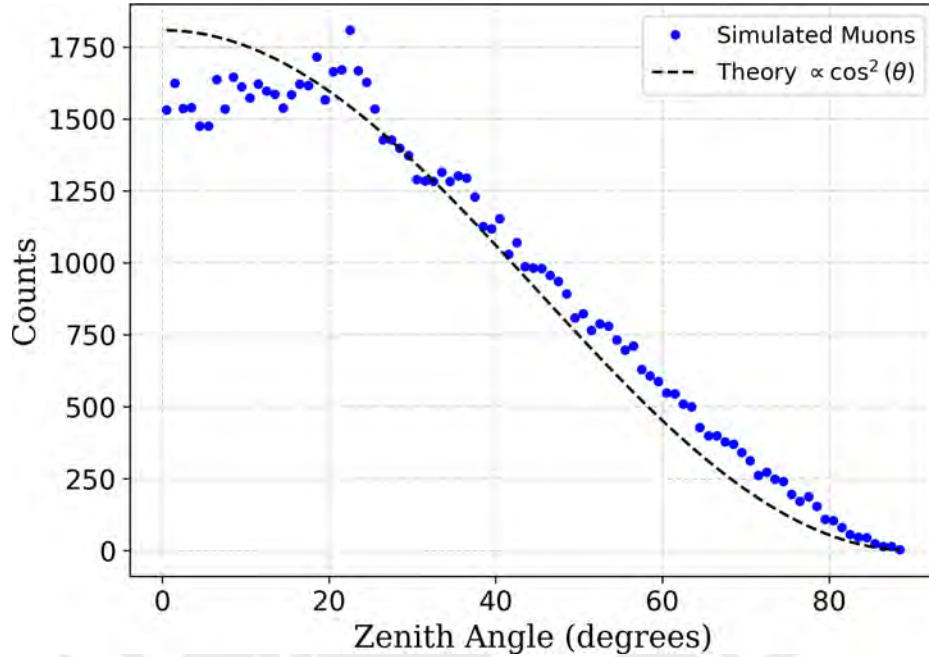


Figure 4.1: Simulated muon angular distributions at ground compared with the theoretical distribution of  $\cos^2\theta$ .

material. It is expressed in  $\text{g}/\text{cm}^2$ . The negative sign represents the energy loss. The distance that a charged particle travels before it loses all its kinetic energy and stops is called *range* ( $R$ ) [38]:

$$R = \int_0^{E_0} \frac{dE}{dE/dX}, \quad (4.3)$$

where the integral is from the initial energy of the particle  $E_0$  until it is at rest. The amount of energy loss depends on the type of particle and the energy at which it occurs. A 10 GeV muon has a range of  $4920 \text{ g}/\text{cm}^2$  approximately in rock, which is 19 m [30].

Fig. 4.2 presents the muon energy loss rate for selected materials, including water, polystyrene, lead, iron, aluminum and concrete, in an energy range of 1 to  $10^9$  MeV. The stopping power values exhibit significant variation for different materials in this energy regime. For instance, water and polystyrene demonstrate remarkable similar energy deposition characteristics, both showing stopping power values compared to the other materials examined. Concrete and aluminum have intermediate stopping power values, while iron and lead exhibit the highest energy deposition due to their greater material density. The density of water is  $1.0 \text{ g}/\text{cm}^3$  and of lead is  $11.35 \text{ g}/\text{cm}^3$ . The comparison clearly shows a direct proportional relationship between material density and stopping power.

The energy dependence of stopping power reveals two distinct regimes. At

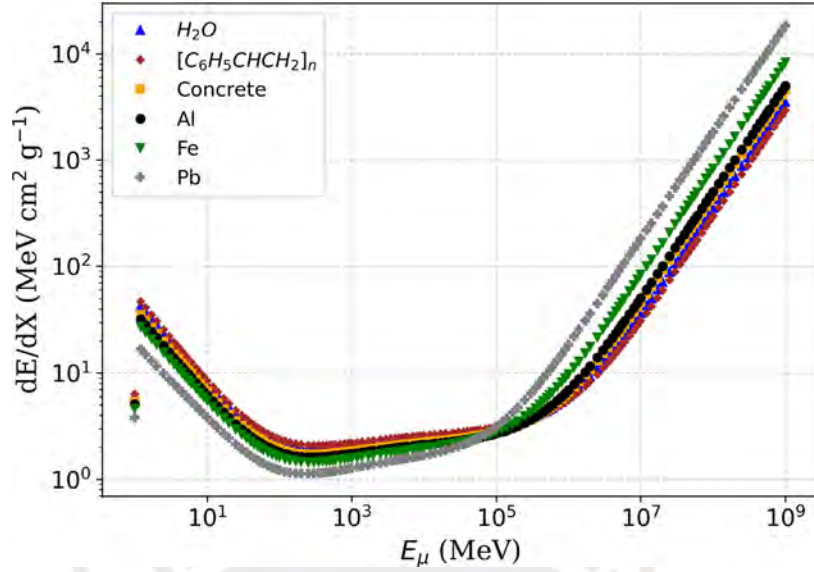


Figure 4.2: Muon energy loss rate for different materials: water( $H_2O$ ), polystyrene( $[C_6H_5CHCH_2]_n$ ), lead (Pb), iron (Fe), aluminium (Al) and concrete. Values are extracted from [59].

lower energy, the stopping power decreases until  $2 \text{ MeV}\cdot\text{cm}^2/\text{g}$ , where it has its minimum value. Beyond  $10^5 \text{ MeV}$ , the stopping power increases with the muon energy afterwards, and the difference between the materials is more noticeable. This energy-dependent behavior is particularly important for understanding the dynamics of muon interaction in various materials [59].

### 4.3.1. Energy Loss by Ionization

Charged particles, such as muons, travel through matter and loss energy by multiple Coulomb interactions with electrons in the medium. For these particles, the most important mechanism is the energy loss by ionization and excitation. The Bethe-Bloch formula describes this process [30], [60],[61]:

$$-\frac{dE}{dX} = Kz^2 \frac{Z}{A} \frac{1}{\beta^2} \left[ \frac{1}{2} \ln \frac{2m_e c^2 \beta^2 \gamma^2 T_{max}}{I^2} - \beta^2 - \frac{\delta}{2} \right], \quad (4.4)$$

where  $K$  is a constant that depends on Avogadro number's, the classical electron radius and the electron rest energy is  $0.307 \text{ MeV}/(\text{g}/\text{cm}^2)$ ,  $z$  is the charge number of the incident particle,  $Z$  is the target charge number,  $A$  is the target mass number,  $\beta = v/c$  is the velocity of the incident particle,  $m_e c^2$  is the electron rest energy,  $T_{max}$  is the maximum energy transfer to an electron,  $I$  is the average ionization energy of the target and  $\delta$  is the density correction.

The total muon energy loss is expressed as follows:

$$\frac{dE_{\mu}}{dX} = \alpha + bE_{\mu}, \quad (4.5)$$

where  $E$  is the muon energy,  $X$  is the amount of matter traversed,  $\alpha$  is the energy loss by ionization, and  $b$  by three radiation processes (Bremsstrahlung, pair production, and photonuclear interactions).

### 4.3.2. Energy Loss by Radiation

The dominant energy loss mechanism for charged particles vary significantly with energy. At lower energies, ionization represents the primary energy-loss process, while radiative effects become increasingly important at high energy. The energy loss of particles by radiation is produced by many physical phenomena, which will be described next.

It is important to emphasize that in this work we will study atmospheric muons at ground, which have GeV energies. At these energies, muons lose a few MeV of energy by radiation. Most atmospheric muons, which arrive at the ground, do not have enough energy to radiate. However, for completeness, we describe pair production, photo-nuclear interactions, Bremsstrahlung, and Cherenkov radiation, all of which become increasingly relevant at higher energies beyond our primary energy range of interest.

#### Bremsstrahlung

The Bremsstrahlung process occurs when a charged particle interacts with a nucleus, changing its trajectory and decelerates and emitting braking radiation. The resulting energy loss depends on both the atomic number ( $Z$ ) of the material and the mass ( $m$ ) of the incident particle [30], following the proportionality:

$$-\frac{dE}{dX} \propto \frac{Z^2}{m^2} E, \quad (4.6)$$

This relation indicates that the energy loss increases linearly with the energy of the particles. Bremsstrahlung becomes significant for electrons at MeV energies. However, for muons the loss energy is significant from 100 GeV onward.

#### Pair Production

Muons lose their energies by creating an electron-positron pair, a process that dominates at an energy range from 0.5 to 10 TeV. The associated energy loss follows the approximately relation [59]:

$$-\frac{dE}{dX} \propto E \quad (4.7)$$

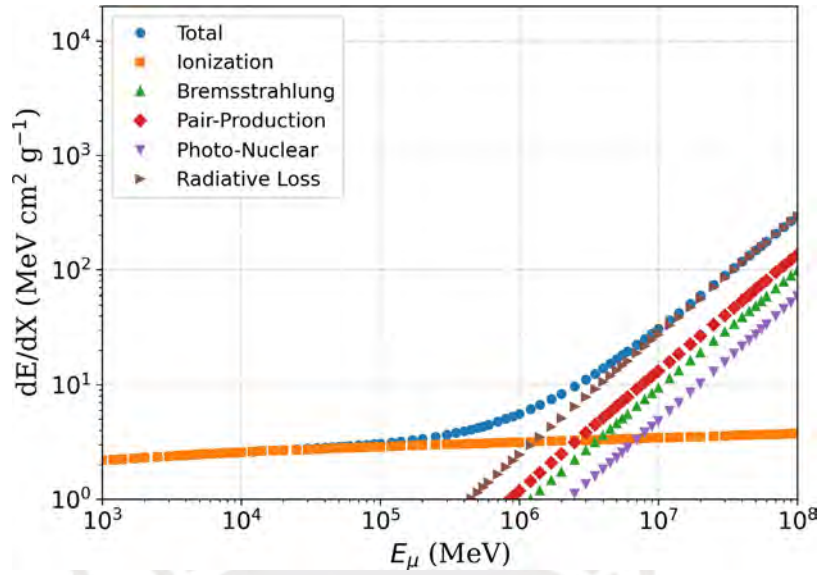


Figure 4.3: Muon energy loss with different contributions for polystyrene [59].

### Photo-nuclear Interaction

Photo-nuclear interaction of muons is an inelastic process of muon-nucleon or muon-nucleus scattering, which can be represented according to this relation:



This process goes through a virtual photon exchange and is important for muon energies greater than 10 TeV [62].

For muons with energies of several hundred GeV, radiative energy losses are more important than ionization losses. Fig. 4.3 illustrates the energy loss of muons with different contributions for polystyrene. We can see the energies for which ionization or radiation is important [59].

### Cherenkov effect

The Cherenkov radiation occurs when a charged particle has a speed larger than the speed of light in the medium (e.g. air, water, or ice). This particle (including muons) loses energy by emitting photons, called Cherenkov radiation [30].

This effect is used for TeV  $\gamma$  astronomy. However, for any charged particle, Cherenkov radiation is emitted at an angle defined by the refractive index  $n$ , which depends on the medium and its speed  $v$ , which is defined by  $\beta = v/c$  [30]:

$$\theta_c = \arccos \frac{1}{n\beta} \quad (4.9)$$

The definition of Cherenkov light implies an energy threshold of 4.5 GeV in air [63] and 160.3 MeV for water and 165.6 MeV for ice. For relativistic particles, the angles are  $\theta_c = 41^\circ$  on ice,  $42^\circ$  on water, and  $1.4^\circ$  in air [30].

## 4.4. Muon Tomography Methods

Muon tomography employs mainly two distinct methodologies [56] that utilize the flux of muons produced by CR interactions in the atmosphere: (1) absorption-based imaging and (2) scattering-based analysis. Nevertheless, the absorption measurements are used to have information about the integrated density along the muon path, and the scattering analysis is used to get the different atomic number of the target material. These complementary techniques have been used in various experiments from multiple disciplines, including in particle physics research, geological investigations, and archaeological studies, as previously discussed in Chapter 1.

### 4.4.1. Absorption

A muon detector measures the muon flux from different directions. These muons are likely to be absorbed by a target along the line of sight. This probability is the basis for the muon tomography method [56]. This method shares conceptual similarities with conventional X-ray radiography. It is based on the dependence between the attenuation of the radiation and the density of the matter traversed. Through careful analysis of attenuation patterns, it is possible to reconstruct a two-dimensional density map of the target [64].

Table 4.1 presents important parameters for the investigation of materials in this study, including: stopping power values, continuous-slowing-down approximation (CSDA) ranges, material densities, and penetration depths corresponding to 1 GeV of energy muons.

The CSDA range is calculated from:

$$R(E) = \int_{E_0}^E (a(E) + b(E)E)^{-1} dE, \quad (4.10)$$

where  $E_0$  is very small. At very high energy:

$$R(E) = \frac{1}{b} \ln\left(1 + \frac{E}{E_\mu}\right), \quad (4.11)$$

where  $E_\mu = a/b$  is the critical muon energy, which is when the electronic losses and the radiative losses are equal.

Material	Atomic number (Z)	Atomic weight (A)	Density [g/cm <sup>3</sup> ]	dE/dX [MeV cm <sup>2</sup> /g]	CSDA Range [g/cm <sup>2</sup> ]	Traversed length [cm]
Air	7.35	14.72	1.205 x 10 <sup>-3</sup>	3.239	5.07 x 10 <sup>2</sup>	421 x 10 <sup>3</sup>
Water	10	18	1.00	3.009	4.73 x 10 <sup>2</sup>	473
Polystyrene	5.6	104.15	1.060	2.895	4.84 x 10 <sup>2</sup>	456.6
Concrete	50.53	100.53	2.300	2.775	5.46 x 10 <sup>2</sup>	237.4
Aluminum (Al)	13	26.98	2.699	2.693	5.77 x 10 <sup>2</sup>	213.8
Iron (Fe)	26	55.845	7.874	2.773	6.40 x 10 <sup>2</sup>	81.3
Lead (Pb)	82	207.2	11.35	3.126	8.17 x 10 <sup>2</sup>	72.0

Table 4.1: Material properties including density, energy loss, CSDA range and traversed length for 1 GeV muons [59].

In an experiment, as in [13], they use effective absorption or transmission  $t(\phi, \theta)$  to measure the ratio between muon flux after passing the object  $N_T(\phi, \theta)$  and without any object or looking at the free sky  $N_{FS}(\phi, \theta)$  obtained with the detector [56]:

$$t(\phi, \theta) = \frac{N_T(\phi, \theta)}{N_{FS}(\phi, \theta)}, \quad (4.12)$$

Many projects have successfully implemented this absorption-based method to investigate large structures. Notable examples include the DIAPHANE and MURAY collaborations [12], which employed three planes of plastic scintillator forming a muon telescope to examine European volcanoes in 2008. Another significant application is the Maya Muon project, developed at the University of Texas. They used portable muon detectors to map the interiors of sealed Mayan pyramids in Belize, Central America [65].

#### 4.4.2. Multiple Scattering

The trajectory of a charged particle traversing matter suffers multiple small-angle deflections, predominantly resulting from Coulomb scattering described by the Rutherford cross section [61]. The Rutherford cross section describes the probability of scattering of charged particles by a target nucleus per unit of solid angle. The Rutherford cross section is derived from classical scattering theory and the Coulomb interaction principles between the incident particle and the target nucleus. The Rutherford cross section is expressed as follows:

$$\sigma = \frac{Z_1 Z_2 e^2}{4\pi\epsilon_0 E \sin^4(\theta/2)}, \quad (4.13)$$

where  $\sigma$  is the Rutherford cross section,  $Z_1$  and  $Z_2$  are the atomic numbers of the incident particle and the target nucleus, respectively  $e$  is the charge of the electron,  $\epsilon_0$  is the vacuum permittivity,  $E$  is the kinetic energy of the incident particle and  $\theta$  is the scattering angle.

This cross section is an important concept for studying the interaction between charged particles and atomic nuclei [66]. However, the global scattering angle is the sum of smaller deflections. Using the central limit theorem, the distribution of these angles can be approximated by a Gaussian distribution with standard deviation [67]:

$$\theta_{MCS} = \frac{19.2 \text{ MeV}}{\beta c p} \frac{X}{X_0} \sqrt{1 + 0.038 \ln \frac{X}{X_0}}, \quad (4.14)$$

where  $p$ ,  $\beta c$  are the momentum and speed of the incident particle,  $X$  is the distance traveled in the material and  $X_0$  is the radiation length.  $X_0$  is defined by [67]:

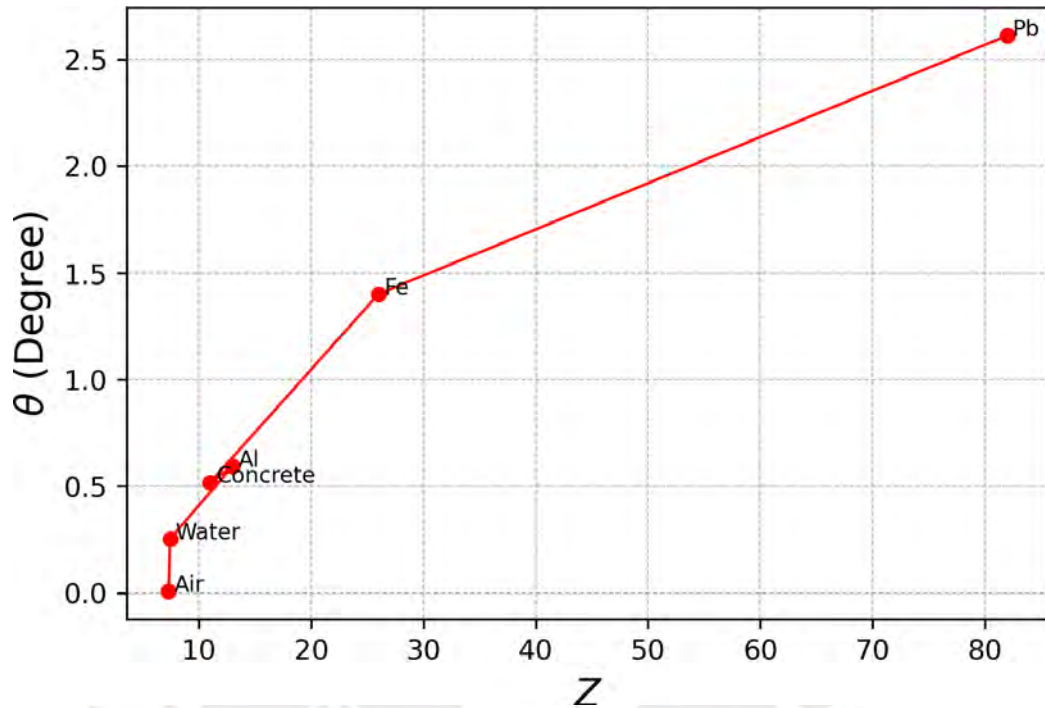


Figure 4.4: Relation between scattering angle and charge number for air, water, aluminum (Al), concrete, iron (Fe) and lead (Pb).

$$X_0 = 716.4 \text{g/cm}^2 \frac{A}{Z(Z+1)} \left( \ln \left( \frac{287}{\sqrt{Z}} \right) \right)^{-1}, \quad (4.15)$$

where  $Z$  is the target charge number and  $A$  is the target mass number.

Radiation length is the length during which the particle loses energy by the radiative process. [56]. Analysis of scattering dynamics reveals that the standard deviation of the deflection angle distribution exhibits a direct dependence on the atomic number  $Z$  according to equations 4.14 and 4.15. Fig. 4.4 demonstrates the relation between the scattering angle and  $Z$  for various elements: hydrogen ( $\text{H}_2$ ,  $Z=1$ ), carbon ( $\text{C}$ ,  $Z=6$ ), aluminum ( $\text{Al}$ ,  $Z=13$ ), iron ( $\text{Fe}$ ,  $Z=26$ ), copper ( $\text{Cu}$ ,  $Z=29$ ) and lead ( $\text{Pb}$ ,  $Z=82$ ). These results were derived fixing all parameters, except for the mass and atomic charge ( $A$  and  $Z$ ). This plot was calculated using the relation 4.14 for each elemental target.

In summary, if we want to study an object using muon tomography, we will need at least two detector planes. One of them above and the other below the object which will be imaged. As illustrated in Fig. 4.5, which reveals the muon tomography imaging techniques (absorption and scattering). The upper detector of this scheme serves to measure the incident atmospheric muon flux, while the lower plane detector detects the presence/absence of muons (absorption method) or their scattering angles after traversing the object (scattering

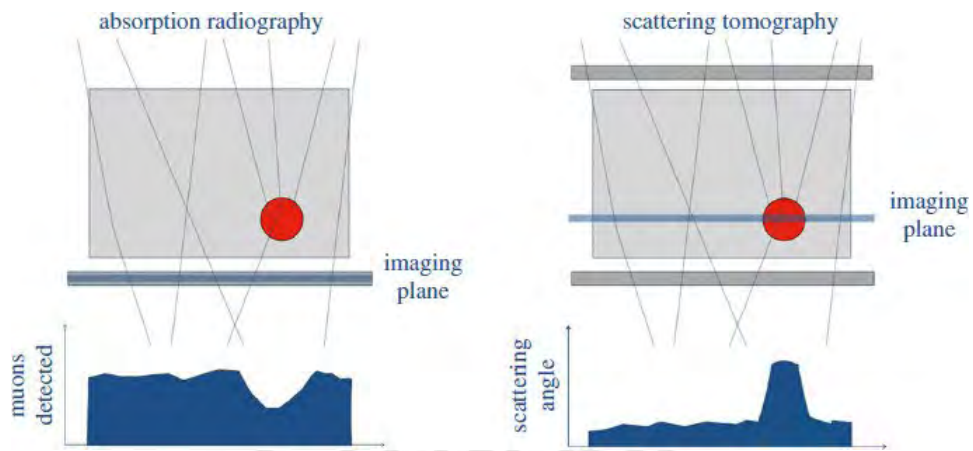


Figure 4.5: Schematic visualization of absorption and scattering methods of muon tomography [5].

method).

Both muon tomography techniques need at least two planes of detectors because with these planes one could construct a two-dimensional absorption image. However, there are some experiments that use three or four detector planes to improve efficiency and resolution and reach three-dimensional images[5]. Fig. 4.5 shows that for absorption radiography we need just one imaging plane, when combined with known muon atmospheric flux data. However, for scattering tomography, we need two imaging planes, since we need to measure the deviation angle.

# Chapter 5

## Muon Detectors

As mentioned in the preceding chapter, there are two main methods in muon tomography: absorption (energy loss measurement) and scattering (angular deflection analysis). The successful implementation of these methods requires specialized detectors designed with a focus on their size, geometry configuration, technological implementation, and performance characteristics (e.g. spatial, temporal, and angular resolution).

For tomographic applications, the experimental configuration typically positions the target volume between multiple detector arrays. These systems record muon events to determine the scattering angle between the incoming and outgoing trajectories or to quantify energy loss. Reconstruction algorithms use this information to generate images of the investigated volume.

In this chapter, for completeness, we summarize the characteristics of different types of detectors that can be used for this purpose, explaining their detection mechanisms. We start with the simple Desktop Muon Detector design, which uses a plastic scintillator and silicon photomultiplier (SiPM). Then, we describe nuclear emulsion detectors, gaseous detectors, multi-wire proportional chambers, resistive plate chambers, micro-pattern gaseous detectors, and Cherenkov detectors. Finally, after considering the different options, we select scintillator-based detectors for this work.

### 5.1. Desktop Muon Detector

The Desktop Muon Detector (DMD) was originally designed and developed by the Cosmic Watch project [49] as a compact muon detection system. Its design incorporates a plastic scintillator with dimensions of  $5 \times 1 \text{ cm}^3$  optically coupled to a SiPM measuring  $6 \times 6 \text{ mm}^2$ . As explained above, this configuration serves to detect an incoming muon through scintillation light conversion. When muons interact with the scintillator, the resulting light pulses are converted into an electric signal by the SiPM. This signal is then processed by a printed circuit board (PCB) which performs amplification and pulse-shaping functions. A microcontroller subsequently measures an event if

the signal peak voltage is above a threshold (value defined in the software). For each recorded event, the system stores multiple parameters, including event number, precise timing information, deadtime, temperature readings, and the average 10-bit ADC value, calculated at SiPM peak voltage [49].

### 5.1.1. Plastic Scintillators

Scintillators represent a class of materials capable of converting ionizing radiation energy into detectable light when excited by the passage of particles. There are many types of scintillators, including liquid and gaseous states, [68], as well as inorganic crystalline systems such as cesium iodide (CsI) and sodium iodide (NaI) [69]. The organic scintillator, used in the DMD, constitutes an alternative category with distinct properties.

The detector in this work employs the commercial organic plastic scintillator BC-408, which is based on polyvinyltoluene ( $[\text{CH}_2\text{CH}(\text{C}_6\text{H}_4\text{CH}_3)]_n$ ) [70] doped with two fluorescent compounds: 2,5- diphenyloxazole (POP) as primary fluor and 1,4-bis [2- (5 - phenyloxazolyl)] benzene (POPOP) as a wavelength shifter. This scintillator is also used in the standard Cosmic Watch detector. The BC-408 implementation in our GEANT4 simulation has a density of  $1.043 \text{ g/cm}^3$  and an elemental composition of carbon (92.26%) and hydrogen (7.74%), exhibiting scintillation yields of 500 photons/MeV. This choice aligns with the general advantage of an organic scintillator, which is easier to manufacture than inorganic scintillators; the latter, although more expensive, typically exhibit superior density and photon yield per unit of energy deposit [71].

The DMD scintillator emits light in the deep-purple spectrum with characteristic emission at 420 nm and absorption cut off near 400 nm [72]. To optimize light collection efficiency, the system incorporates several design features, such as an optical gel between the scintillator and SiPM which minimize photon reflection losses, while an aluminum foil wrapping reflects the escaping photon back into the detection medium. A final outer layer of black electrical tape ensures complete light protection, as illustrated in Fig. 5.1 [71].

On the other hand, when charged particles impact the scintillator material, the amount of light emitted depends on their incident energy and the dimensions of the material [71]. However, there is an experimental formula derived from a fit by Birks, which shows the non-linear relationship between the amount of light produced and the energy deposited. This relation is explained by the transfer of energy to molecules that have been damaged causing them to release the received energy through non-radiative means. The following equation gives the light yield per unit of path length [73]:

$$\frac{dL}{dx} = S \frac{\frac{dE}{dx}}{1 + kB \frac{dE}{dx}}, \quad (5.1)$$

where  $S$  is the normalization factor,  $k$  is the probability of energy transfer,  $B$  is the proportionality constant to determine the number of damaged density

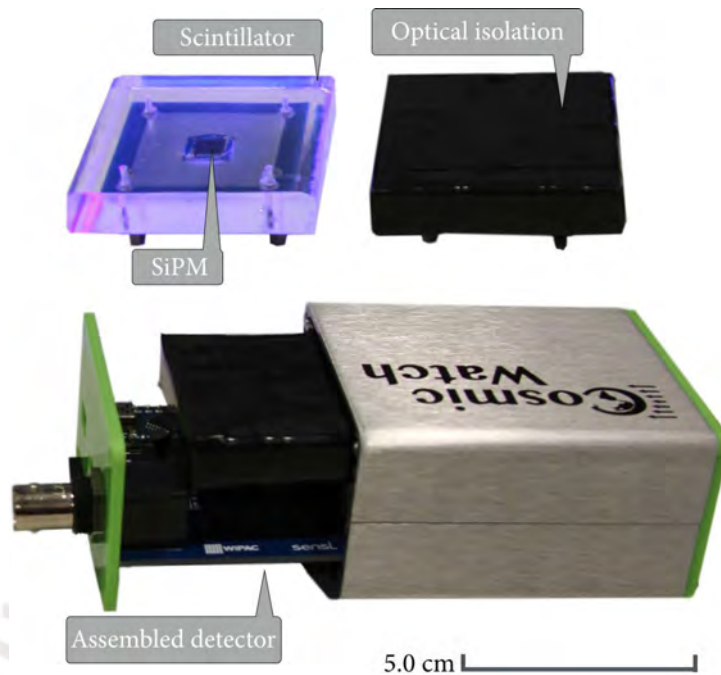


Figure 5.1: Upper left: Plastic scintillator mounted on the SiPM, upper right: optical isolation and down: complete detector assembly in Cosmic Watch Desktop Muon Detector [49].

of the material, and  $dE/dx$  is the stopping power (energy loss by unit length). This equation is applicable primarily at low energy [73].

Ideal scintillators are characterized by high efficiency, linear behavior, transparency to their own emission wavelength, short decay time, and refraction index 1.5 for efficient optical coupling with SiPMs [74]. The light emitted by the scintillator can be read when it is coupled to a SiPM [74], a PhotoMultiplier Tube (PMT) or other light-sensitive devices.

There are different geometries for plastic scintillators, such as square, rectangular, or triangular bars. It is possible to use arrays of several plastic scintillators to cover a large area [56]. This work utilizes such an approach employing an array of DMDs.

### 5.1.2. Silicon Photomultipliers

A Silicon PhotoMultiplier (SiPM) is a photosensor that detects light. It is characterized by the detection and counting of photons with high resolution and sensitivity [75]. It requires only low reverse bias voltage, meaning an inexpensive DC-DC booster can be used to power the circuit.

The detector used in the DMD is the On Semiconductor MicroFC 60035 C-Series, which is most sensitive in the 450 nm range [71].

A SiPM consists of hundreds or thousands of microcells or pixels of silicon

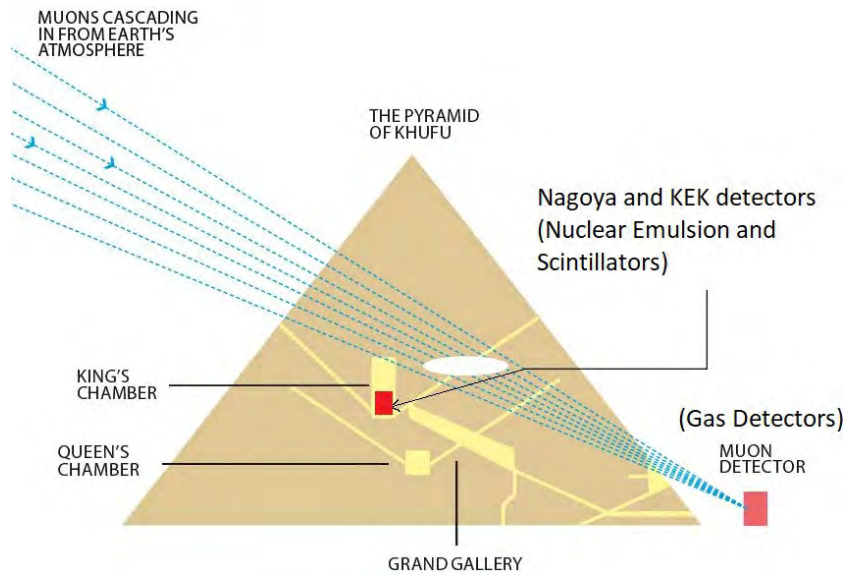


Figure 5.2: Schematic Visualization of Khufu's Pyramids showing its parts and the location of the detectors [77].

in P-N junctions or diodes. Electrons move to the P-side and holes move to the N-side[68]. When an electron breaks loose and becomes free, it leaves a hole. This hole is similar to a bubble in liquid [76].

The photons travel through a region known as the depletion region, where the electron and hole reunite. The photon transfers energy to the electron, causing it to move and generate an electrical current and field. The field ionizes the atoms in the surrounding area, leading to an avalanche of electron-holes pairs. This process eventually produces a detectable signal from a single photon [68].

## 5.2. Nuclear Emulsion Detectors

A nuclear emulsion is a photographic film capable of detecting minimum ionizing particles like muons. An example of this detector is the one used in the muon tomography of the Khufu's Pyramid in Giza, Egypt [8]. In Fig. 5.2 we see a schematic visualization of the pyramid including the location where the detectors were installed.

This detector can record the three-dimensional trajectories of charged particles passing through it. An optical microscope can help reconstruct the muon tracks by identifying the coincidence between the films [8].

This detector was configured as six packed nuclear emulsion films, each with an area of 30 cm x 25 cm. These films are fixed in two groups of three films each, placed between a rubber sheet and two aluminum plates. Fig. 5.3

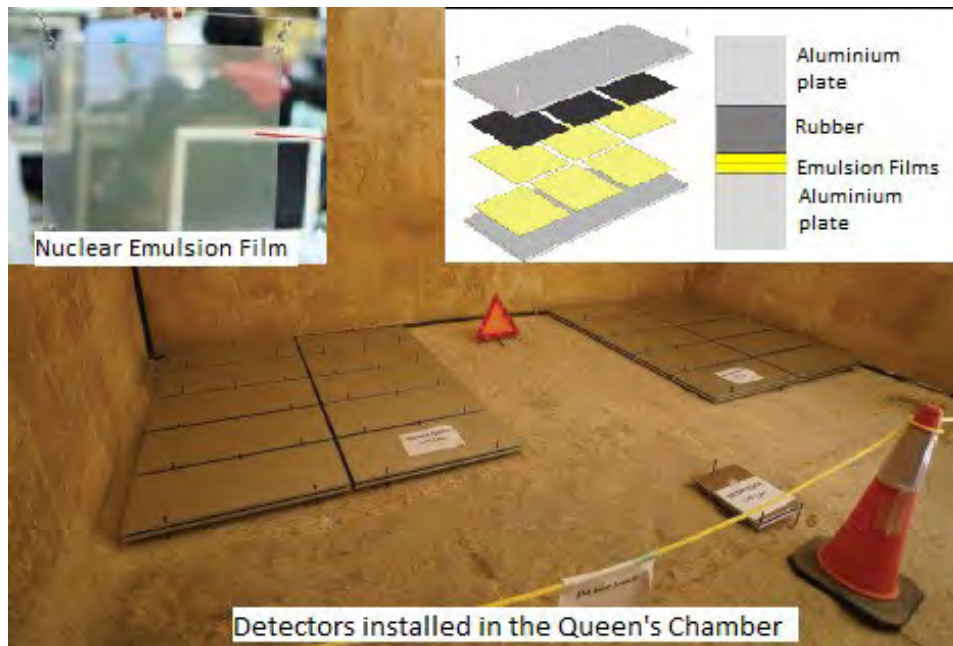


Figure 5.3: Top left: isolated nuclear emulsion films. The main photo shows the detectors installed in the Queen's chamber inside the Khufu's pyramid [8].

presents, on the top left, the isolated nuclear emulsion film, on the top right, the nuclear emulsion packed with a rubber sheet and aluminum plates pressing them. Furthermore, in the lower plot, we can see that the plates are grouped together to form the detectors [8].

The spatial resolution of these films is a few microns [56] and the mean angular resolution is 8 mrad ( $0.46^\circ$ ) [8].

### 5.3. Gaseous Detectors

This type of detector is a good option when high angular resolution is an important parameter. When a muon passes through this detector, it ionizes the gas and liberated electrons are captured by the anode under the influence of an electric field. The geometry most commonly used for these detectors is cylindrical. The anode wire can be approximately 100 microns in diameter. A high electric field produces avalanche multiplication near the anode [56].

One of the advantages of these detectors is their high resolution and large detection area, as the gas volume can be expanded. The spatial resolution can be further improved by using techniques such as multi-wire chambers (which use segmented cathode strips for readout) or drift chambers (which measure the electron drift time from the muon track to the anode wire) [56].

We will briefly explain some examples of gaseous detectors, for instance, Micromegas, multi-wire proportional chambers (MWPC), resistive plate cham-



Figure 5.4: Schematic visualization of WatTo muon telescope based on Micromegas technology [79].

bers (RPC), and gas electron multiplier (GEM).

### 5.3.1. Micromegas

Micromegas stands for MICRO MESH Gaseous Structure. It is a micro-pattern gaseous detector, designed with an anode segmented into metallic strips with a pitch sustained by pillars. The gap between the cathode plane and this mesh is called the drift region and is filled with a gas mixture Ar : CO<sub>2</sub> [78].

The WatTo experiment [79] is an example of a Micromegas telescope for muon detection (see Fig. 5.4). They built four resistive multiplexed Micromegas detectors with self-triggering electronics to reconstruct muon trajectories using double tracks. These detectors consume little electricity and are read out with a single Front-End Unit. They achieve a high spatial resolution due to their high granularity, with each detector providing a spatial resolution of 300 $\mu$ m and an angular resolution of 0.35 mrad (2°). Generic multiplexing is used to reduce power consumption while maintaining good accuracy.

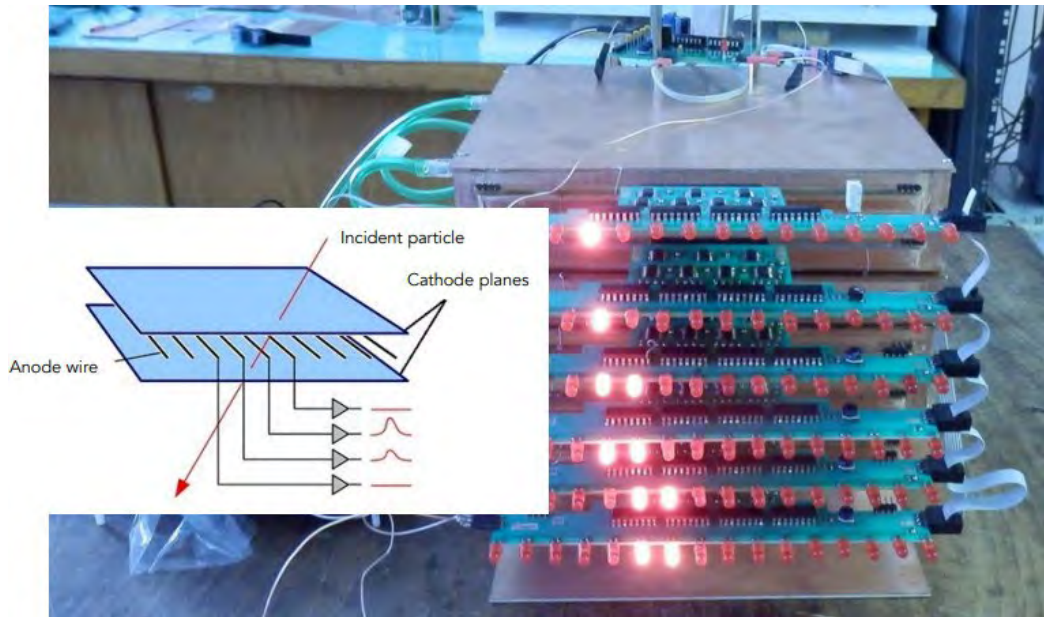


Figure 5.5: Basic scheme of a MWPC [83] and real MPWC chambers showing a muon trajectory [82].

### 5.3.2. Multi-wire proportional chambers

A Multi-wire proportional chamber (MWPC) [80] consists of a set of parallel thin anode wires and a cathode plane. When charged muons pass through the detector, the electric field increases near the wires, causing gas ionization. This gas is typically argon mixed with carbon dioxide. Then, electrons released in the ionization or avalanche process are attracted to a nearby wire, generating a current that can be amplified and registered. Their position resolution is about 1 cm. According to [80], this resolution allows the particle trajectories to be clearly observable. In [81] a spatial resolution of hundreds of microns is mentioned.

Fig. 5.5 presents six MWPC chambers showing the muon trajectory with lights on [82], along with a basic schematic of the detector [83].

### 5.3.3. Resistive Plate Chambers

The Resistive Plate Chamber (RPC) is a muon tracker with high detection efficiency, good temporal resolution and good spatial resolution. It is constructed as a large planar capacitor with two parallel high bulk resistivity electrode plates, separated by a gap of a few millimeters filled with a gas mixture. This gas mixture defines the time resolution of the RPC (4ns) and the spatial resolution (approximately  $100\mu\text{m}$ ). The electrodes are made of a phenolic-melaminic laminate [84].

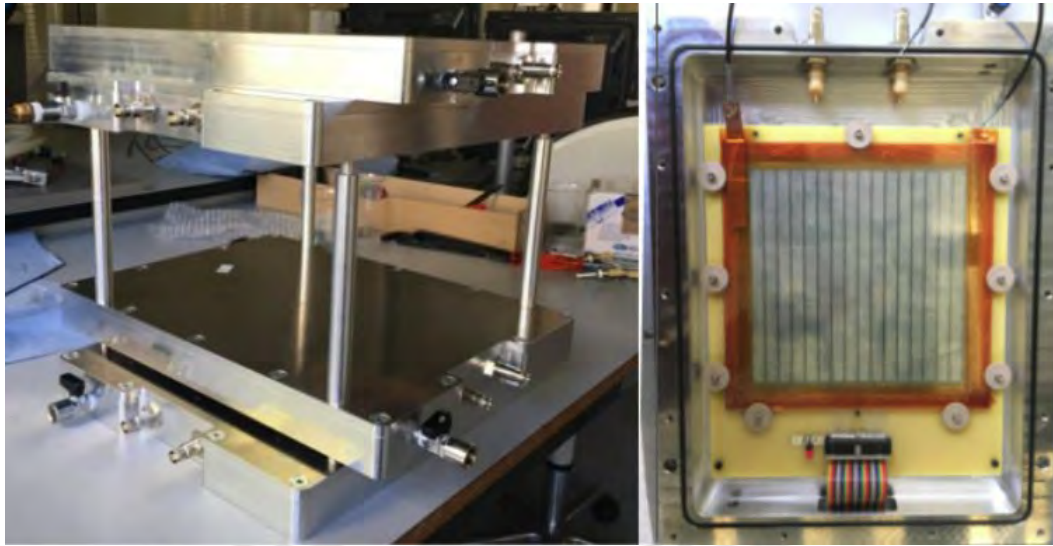


Figure 5.6: Muon telescope based on RPC and one of the RPC detectors inside its casing [85].

Similarly to other gaseous detectors, when the muon passes through the gas, it ionizes the gas and initiates an electron avalanche in the presence of an electric field. The electrodes have high resistivity, which is much greater than that of discharge processes. The ionization is amplified exponentially with distance from the anode. This amplification allows one to distinguish the signal from the noise. This detector enables 2D localization of the signal because the signal distribution is isotropic [84].

Fig. 5.6 presents a muon telescope based on RPC technology and one RPC detector inside its casing [85].

#### 5.3.4. Gas Electron Multiplier (GEM) Detectors

GEM detectors are micro-pattern gas detectors. Their important components are a drift cathode, GEM foils, and a gas mixture that fills the volume of each sealed detector [86].

This detector operates as follows: A charged particle ionizes the gas as it passes through the detector. The liberated electrons are then accelerated through a series of GEM foils, producing an avalanche of electrons, which means amplifying the original signal into a measurable current. Each detector has a drift cathode made of Kapton, a 50  $\mu\text{m}$  thick polymer foil. A negative electric potential is applied to one side of the drift cathode, attracting the positive ions generated during ionization. These ions recombine with electrons before they can propagate [86].

These detectors are typically filled with argon because it is inexpensive, easy to ionize, and recovers quickly from electron avalanche. However, other

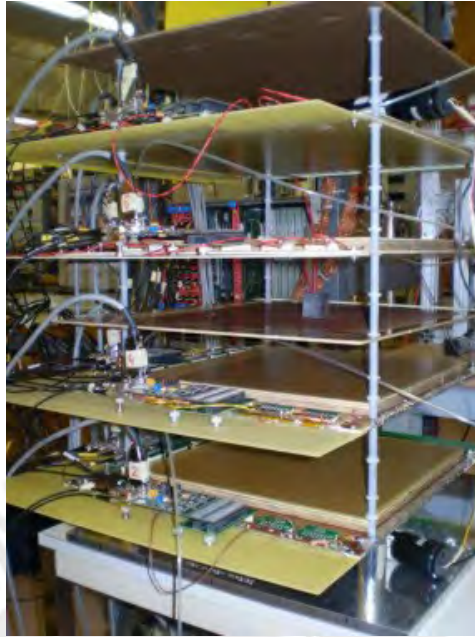


Figure 5.7: Muon tomography station prototype using GEM detectors from [86].

gases can also be used [86]. GEM detectors offer a spatial resolution of 70–100  $\mu\text{m}$  and a time resolution of 10 ns [84].

Fig. 5.7 presents a prototype muon tomography station from [86] with two GEM detectors that image a small block of lead in the middle of each other.

## 5.4. Cherenkov Detectors

A Cherenkov detector operates using the effect of the same name, the Cherenkov effect. This occurs when a charged particle traveling through water, ice, or other materials moves at a speed greater than the light speed in that medium. In this situation, photons are produced. These photons, called Cherenkov light, can be detected and recorded via the photoelectric effect, by photomultiplier tubes (PMTs). With these detectors, one can reconstruct the energy in the incidence direction of the muons produced in EAS [41].

However, some muon detectors use combined techniques for muon tomography. For example, the Muon Telescope (MuTe) [10] is a hybrid detector. MuTe uses two techniques, the first employing two scintillation panels for particle tracking, and the second using a Water Cherenkov Detector (WCD) for filtering cosmic background radiation from the extensive air shower of particles. Fig. 5.8 shows the schematic structure of the hybrid Muon Telescope - MuTe [87].

The aperture angle and the angular resolution change with the distance



Figure 5.8: Structure of the Muon Telescope MuTe [10].

between the scintillator panels. For example, for a distance of 150 cm, the total angular aperture is 1.3 rad (74.4°) and the angular resolution is 53 mrad (3°). In addition, the spatial resolution depends on the distance between the detector and the object to be scanned with muon tomography. On the other hand, the WCD detects charged particles with an energy resolution of 0.72 MeV [10].

Finally, different detectors can be used for muon tomography. For example, nuclear emulsion, scintillator, and Micromegas were used to scan the Khufu pyramid [8]. Other detectors are used to scan volcanoes. For example, the MWPC-Muographic Observation System (MMOS) uses muon detectors based on Multi- Wire Proportional Chamber (MWPC) technology to scan the vicinity of the Minami-dake crater of the Sakurajima volcano [11]. In Colombia, there is a hybrid muon detector called MuTe, which uses a Cherenkov tank and scintillators to scan volcanoes of the Colombian Andes [10].

## 5.5. Detector design selection

Now we compare the detectors mentioned before and show the selected design of this work. For this comparison, we show the following summary Tables 5.1 and 5.2:

Characteristics	Nuclear Emulsion	Micromegas	MWPC	RPC	GEM
Detection Medium	Silver Bromite Crystal	Ar : CO <sub>2</sub>	Ar : CO <sub>2</sub>	Ar : CO <sub>2</sub>	
Photons Detection	photographic film	*	wires	*	*
Detector Dimensions	30 × 25 cm <sup>2</sup>	50 × 50 cm <sup>2</sup>	48 × 48 cm <sup>2</sup>	32 × 48 cm <sup>2</sup>	10 × 10 cm <sup>2</sup>
Spatial Resolution	microns	300μm	microns	100μm	70–100 μm
Mean Angular Resolution	8 mrad (0.46°)	0.35 mrad (2°)	2.6 mrad (0.15 °)	15 mrad	*

Table 5.1: Muon detector's characteristics. The symbol \* means not available or not apply

Characteristics	DMD	MuTe	This work
Detection Medium	Plastic scintillator	scintillator panels	Plastic scintillator
Photons Detection	SiPM	PMT	SiPM
Detector Dimension	5 × 5 × 1 cm <sup>3</sup>	370 × 120 × 120 cm <sup>3</sup>	48.4 × 48.4 × 22 cm <sup>3</sup>
Spatial Resolution	D-O	D-O	D-O
Mean Angular Resolution	26.18 mrad (1.5°)	53 mrad (3°) (for 150 cm)	17 mrad (1°) (for 250 cm)

Table 5.2: Muon detector's characteristics. D-O: Depends on the distance between the detector and the object to scan. The values of this work were based on [26].

After considering all these characteristics, we chose to design the detector based on plastic scintillators and SiPMs, as this approach is easier to implement than other alternatives. This design is easily transportable and does not require maintaining a specific temperature, unlike gaseous detectors (such as Micromegas, MWPC, RPC, and GEM) which often need to be kept at low temperatures and require careful handling. Similarly, water-based detectors, such as MuTe, are more complicated to handle.

Our detector design shares a foundational concept with an advanced system like the MuTe telescope, which also employs scintillation panels. However, our approach introduces key innovation in compactness and focus: while MuTe relies on a large WCD combined with sizable scintillation panels to filter background radiation from EAS, our design achieves portability and cost efficiency through a more integrated and geometrically optimized scintillator-SiPM array. This allows us to maintain performance in muon tracking and material differentiation without requiring an additional background rejection system, making our detector uniquely adaptable for field applications where mobility and simplicity are critical.

Physical dimensions, spatial resolution, and mean angular resolution are important factors to consider. Gaseous detectors have dimensions similar to each other. The MuTe detector is the largest, but gaseous detectors generally offer better mean angular resolution. The spatial resolution for these detectors is on the order of hundreds of micrometers, however, for our detector, the spatial resolution depends on the distance of the object and the detector, the same for MuTe.

For this work, we have implemented a GEANT4 simulation of the detector (see Chapter 6)). This design consists of an array made up of 8 unit detectors. Two planes of this array form a sub-detector. We created these arrays to improve the detection area and achieve an angular resolution of approximately 17 mrad ( $1^\circ$ ), which is obtained when the two planes are separated by 20 cm and the object of study is placed 250 cm from the detector [26].

# Chapter 6

## Detector Design and Simulation

In this chapter, we will describe the detector designed for muon tomography, analyzing the two methods described in Section 4.4: absorption and multiple scattering. The design will specify the dimensions of the geometry of the experimental setup, which includes an object (i.e., a block) under study, as a simplified version for tomography. We also describe the simulation chain based on our detector.

The simulation begins by calculating the number of showers per hour, taking into account the characteristics of Lima, described in Chapter 3, to obtain a realistic CR flux. This simulation was performed using CORSIKA and served as input for the detector simulation in GEANT4.

We designed the detector and the object of study and simulated them in GEANT4. We studied and selected the optimal geometric parameters for the detector configuration to improve the resolution and the ability to differentiate between different materials.

### 6.1. Detector Design and Geometry

Our detector takes the DMD as a reference for the basic detection unit, as described in Section 5.1. The unit detector is formed by a plastic scintillator of  $5 \times 1 \times 1 \text{ cm}^3$  coupled to a SiPM light sensor with an area of  $66 \text{ mm}^2$ .

However, for this application, we aim to improve both the angular resolution and the detection area. Therefore, we designed planes (see Fig. 6.1) consisting of arrays of  $8 \times 8$  arrays of unit sensors. Each unit sensor is housed within an aluminum box to provide isolation and obtain precise muon track identification. This configuration results in a whole plane array that covers  $48.4 \times 48.4 \times 1 \text{ cm}^3$  [26]. The detector design prioritizes practical implementation using current technology.

To reconstruct the direction of the muon track, a minimum of two such array planes is required to form a single sub-detector. Since the objective is to reconstruct the change in trajectory of the muons (i.e., scattering angle), the complete tomographic system comprises two sub-detectors. These are placed

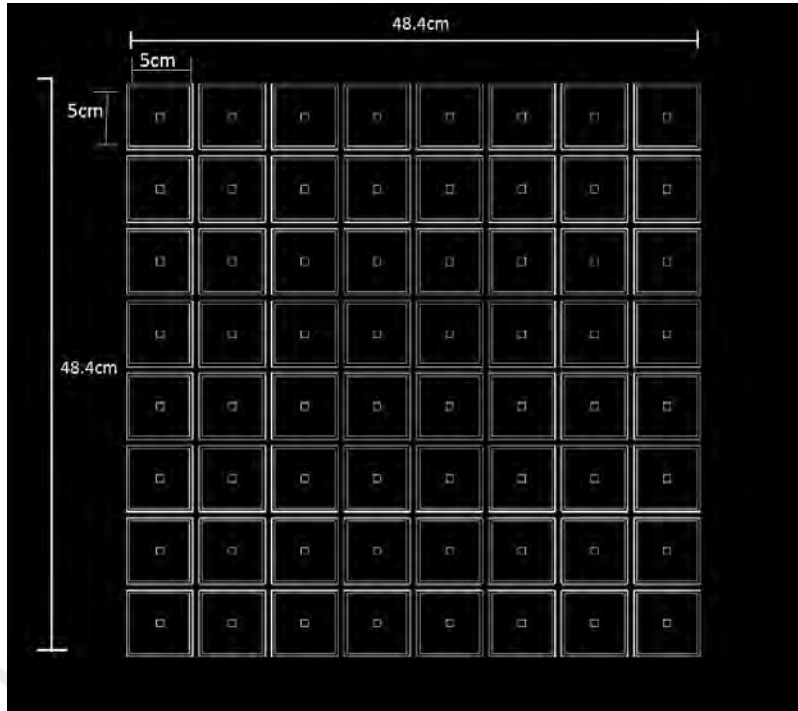


Figure 6.1: Plane array of sub-detector showing its dimensions [26].

before and after the object under study, as illustrated in Fig. 6.1 [26].

Our goal was to identify the distance configuration that maximizes material differentiation. For this study, the parameters  $d$ ,  $D$  and  $D'$  were maintained at fixed values while systematically varying the width of the object  $W$ .

The distance between two planes is  $d = 20$  cm (see Fig. 6.2), selected to ensure the portability of the system. This compact design facilitates transportation between measurement locations [26].

The baseline distances were established as follows:  $D' = 60$  cm (from the object to the first sub-detector) and  $D = 260$  cm (from the object to the last sub-detector as seen in Fig. 6.3). Throughout our parameters studies,  $d = 20$  cm remained constant. However,  $D$  and  $D'$  were adjusted relative to the position of the object to maintain the same value according to the widths of the object. We determined the optimal geometric configuration for  $D$  and  $D'$  to achieve a target angular resolution of  $1^\circ$ .

To achieve optimal resolution and material identification capabilities, we optimized the geometrical parameters of the measurement setup. These key parameters under investigation are the distance between the two planes of each sub-detector  $d$ , the distance from the first sub-detector to the object  $D'$ , the distance from the object to the final sub-detector  $D$ , and the width of the object  $W$  itself (see Fig. 6.4) [26].

To study an object with muon tomography, we simulated a system with two identical sub-detectors, one positioned before and one after the object.

Each sub-detector is compound by two-planes of array, which serve to reconstruction the muon trajectory. The intrinsic angular resolution for a single sub-detector, based on the distance  $d$  between its two planes and the pixel size, is approximately  $14^\circ$ . However, when calculating the resolution for the entire system using the large separation  $(D' + D)$  between the front and rear sub-detectors relative to the object, the angular error for reconstructing the scattering angle within the object improves significantly to approximately  $1^\circ$  [26].

The angular resolution is derived from the spatial resolution of a single pixel with a length of  $h = 5$  cm. Assuming a uniform sensitivity, the positional standard deviation is  $\sigma_x \approx h/\sqrt{12} \approx 1.44$  cm. This yields a statistical angular resolution of  $\sigma_\theta \approx \frac{\sqrt{2}\sigma_x}{d} \approx 5.8^\circ$  for a single sub-detector. Geometrically, the maximum angle subtended by a pixel in one sub-detector is  $\arctan(h/d) \approx 14^\circ$ . For a complete two sub-detector system, the increased lever arm  $(D' + D)$  improves the resolution. The statistical uncertainty improves to  $\sigma_\theta \approx \frac{\sqrt{2}\sigma_x}{D'+D} \approx 0.4^\circ$ , while the geometric uncertainty reduces to  $\arctan(h/(D' + D)) \approx 0.9^\circ$  [26].

Based on these calculations, we conservatively adopt a final angular resolution of  $1^\circ$  for our analysis. This value represents a practical balance between performance and cost. Increasing the detector separation would reduce the muon flux, and deploying a smaller pixel would necessitate a prohibitively large number of detection units.

The object of width from 0.5 to 2.5 m is a simplification of spent fuel casks, shipping containers or nuclear waste containers [88, 89, 90]. In spite of that, greater objects can also be analyzed. For example, building, large mountains, or archaeological remains, as we described in Chapter 5. According to other works, such as that of Gomez in 2019 [91], the scattering method is more sensitive for small objects, but it is necessary to install muon detectors on both sides of the object and use longer measurement times. In addition, there are other examples of small objects on the order of the object we studied in this work, such as statues and archaeological artifacts, art pieces, museum objects like ancient vessels or ceramic pieces, electronic devices, and laboratory material samples.

The object in these simulations is a block of different materials and smaller dimensions, which will be described later. This approach has limitations since real objects are more complex; for example, they can have structures with holes, materials combinations, and different geometries.

In addition, to increase the angular coverage of recorded muon tracks, the sub-detector located after the object could be rotated by approximately  $90^\circ$  around it as shown in Fig.6.5. This would require a rotating mechanism that can be controlled remotely. This capability would allow the sub-detector to be positioned on one side of the analyzed object and then rotated to the opposite side, which is shown in Fig.6.6, enabling the detection of muons passing through the object from different incident angles.

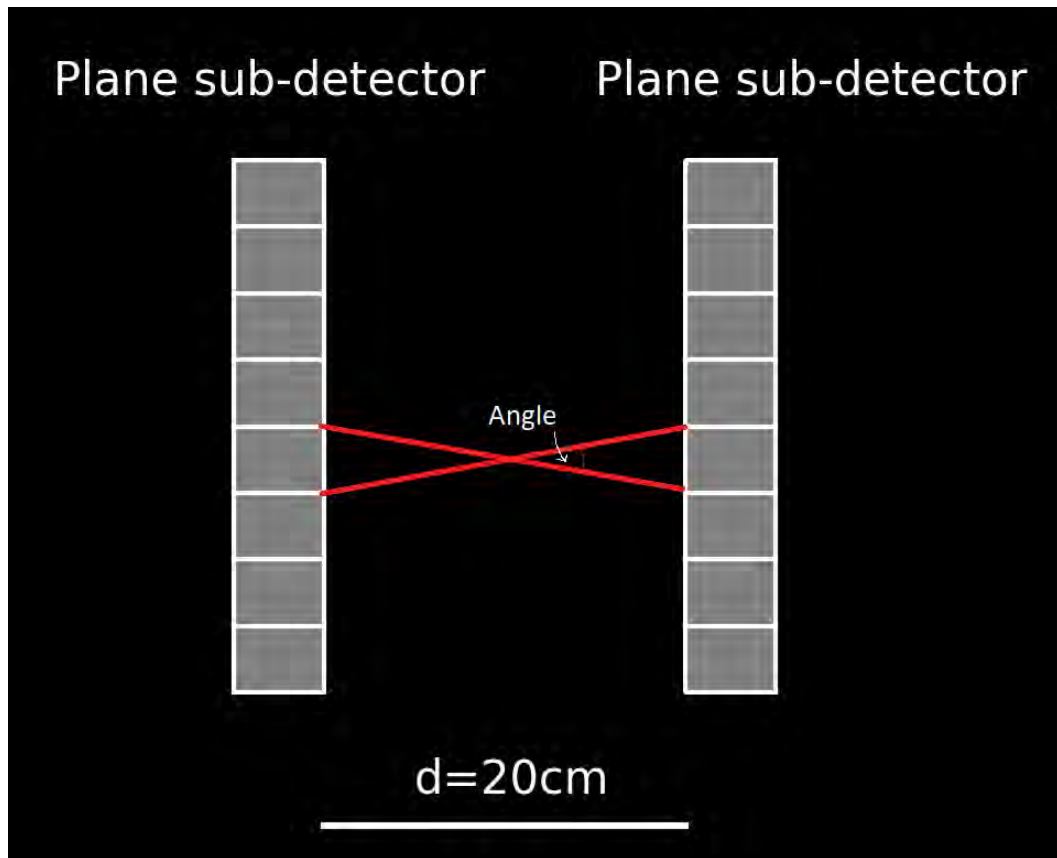


Figure 6.2: Distance between two planes of a sub-detector and the angle formed between unit-detectors, which measure  $\approx 14^\circ$ .

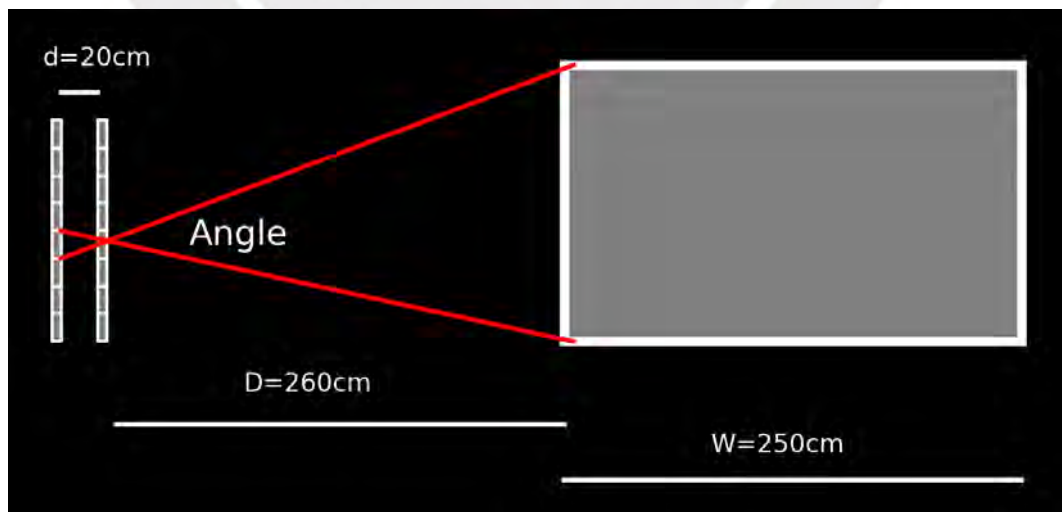


Figure 6.3: Distance between the detector and the object and the angle formed between unit-detectors and the block, which measure  $\approx 0.9^\circ$ .

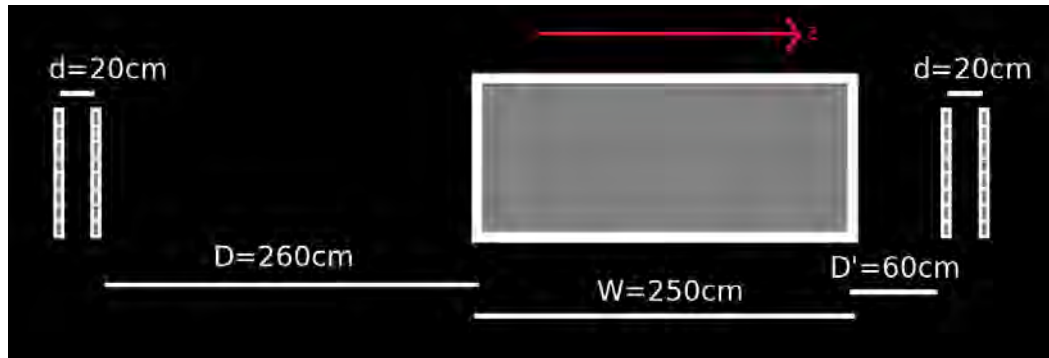


Figure 6.4: Detector design simulated in GEANT4 showing two planes or arrays based on plastic scintillators and SiPMs, where the right planes are the sub-detector that receive the muon flux from the atmosphere, the left planes are the detector that receive the scattering or absorption of muons after passing through the object, which is in the center of the picture.  $W$  is the width of the object or block of different material,  $D$  is the distance between last sub-detector and the object,  $D'$  is the distance between first sub-detector and the object and  $d$  is the distance between two planes. Notice that the muon track comes from  $Z$  axis direction.

Moving or rotating a muon detector is important because it allows for more comprehensive measurements of the muon flux from various directions. This provides valuable information about the internal composition and density structures through which the muons pass. However, a practical consequence of this rotation scanning in a real measurement is a significant increase in the required data acquisition time to cover the entire angular range of interest.

## 6.2. GEANT4 Simulation

GEANT4 (GEometry ANd Tracking) is a software toolkit to simulate the passage of particles through matter (i.e., different materials). It was developed by CERN [29]. Using GEANT4, we can define the particles, detector material, geometries, and physics interactions through libraries, generating an output with information about the particles that pass the objects and detectors. We will describe in detail the process of this simulation.

We have used two methods to create input data: (1) defining one thousand muons with a specific energy and direction, which is used to learn about the tracks, absorption and deviation and (2) using the output from CORSIKA simulations, which is used to obtain more realistic results.

In the first case, one thousand muons were injected with 4 GeV (that is, the mean energy of muons arriving at the ground, as described in Section 2.4.1), starting 1 cm before the first sub-detector. We defined a single direction,

perpendicular to the detector planes, to increase the statistical likelihood that particles pass through both the object and the detectors.

In the second case, we used the output from CORSIKA. In Chapter 3, we described the parameters used to obtain a realistic particle flux at the ground level. As an example, we considered specific parameters for a 1-hour measurement period in Lima. We input into Geant4 the initial information (e.g., particle type, position, momentum, shower ID, and the primary particle ID) for all particles generated by CORSIKA. Based in the results of CORSIKA simulation, we defined the momentum direction, the initial energy, and the position of the secondary particles. In addition, we use the shower ID to classify particles according to their originating shower. Fig. 3.6 shows the distribution of radii and energy of the secondary particles generated with CORSIKA (i.e., muons, electrons, photons and hadrons). It is important to note that muons are more energetic and arrive in a larger number than other particles at ground level. For this reason, we have chosen to include only muon in our simulations.

However, to obtain a larger number of useful events without increasing the CORSIKA production time, we modified the original particle directions from the CORSIKA output. Instead of considering particles arriving from all directions, we set a single direction for all muons aligned with the line connecting the detectors and the object. This modification reduced the computational time required to achieve the statistically significant result. The consequence is that the real observation time will be larger than the simulated one. This will be calculated in the next chapter.

### **6.2.1. Detector Definition**

We defined the experimental setup in GEANT4 by specifying its geometry, materials, and sensitive regions. We also define the physics processes, which are described in 4.3. These processes include: photo-nuclear interaction, Compton scattering, Rayleigh scattering, multiple scattering, the photoelectric effect, ionization, Bremsstrahlung, pair production, elastic and inelastic scattering, particle decay, gamma nuclear physics, and optical physics.

We created the environment (i.e. the “world”) around the detector using  $G4_{AIR}$ . We selected the following materials for the test block: lead (Pb), iron (Fe), aluminum (Al), concrete, water, and air. These objects were scanned exclusively with atmospheric muons. We implemented a test object as a rectangular parallelepiped-shaped block, with a constant cross-section of  $80 \times 80$  cm<sup>2</sup> on the X and Y axes and a variable length on the Z axis. We tested different lengths: 50, 100, 150, 200 and 250 cm to determine the size range within which materials could be effectively distinguished.

We used plastic scintillator and silicon to simulate the sensitive material in the detector and the SiPM (silicon photomultiplier), respectively, as described in Chapter 5. The dimensions of the unit detector were 1 cm on the z-axis and 5 cm on the x- and y-axes. The detector casing material was defined as

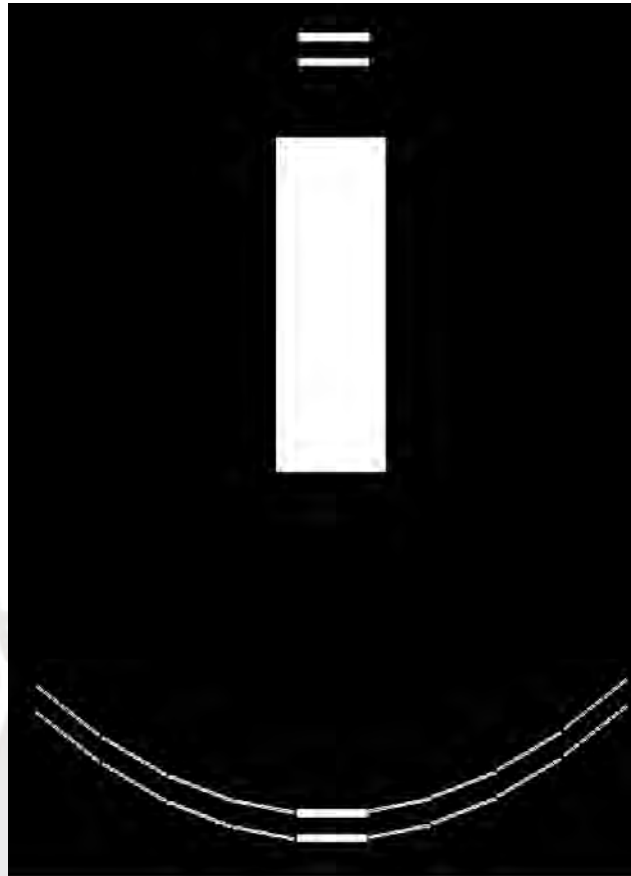


Figure 6.5: Tomographer designed in GEANT4 and geometric array of detectors with the third and fourth planes turning  $90^\circ$  approximately around a central point.

aluminum, with a wall thickness of 0.05 cm surrounding the sensor. The key component of the detector is the polystyrene-based plastic scintillator. We define it with two components: Hydrogen (H) with mass fraction 0.77 and carbon (C) with mass fraction 0.92. We also added the optical and scintillation properties of the plastic scintillator, including its refraction index of 1.58, absorption length of 210 cm, photon energy yield, and scintillation yield [92].

### 6.2.2. Detector Simulation

First, we define the materials and then the structures of the detector. We started defining the position of the two sub-detectors, of the object and the object dimensions. In addition, the plane arrays that form the sub-detectors were constructed from multiple copies of the unit-detector.

We read the output of the CR flux simulated in CORSIKA, as described in Chapter 3. We define the CORSIKA ID of the generated particles (i.e., particle type), their position, momentum, and shower ID to introduce these data into

our GEANT4 simulation. With `StackingAction` and `SteppingAction`, we save important data to analyze after the simulation. These data correspond to the number of optical photons detected in the detectors, as well as the number of events, track ID, positions, and momentum, to identify each particle that passes through the detectors and the object.

Furthermore, for a comprehensive muon tomography scan of an object, it is necessary to move the sub-detector around the object at various orientations. This movement allows us to collect muon data from different angles, providing a better reconstruction of the internal structure of the object. The resulting image could be more complete and accurate. In this scenario, the two planes that follow the object are rotated by approximately  $90^\circ$  around the object.

To facilitate the rotation of the detector array, a mechanical system would need to be employed. This system would have motors, gears, and a robust framework to support movement of the array. Using a controlled motor operation, we would achieve precise and synchronized rotations of the two planes.

We would also need accurate data acquisition, calibration, and alignment of the detector. Before the scanning process, the detector would be calibrated to characterize the response of the scintillator and SiPMs inside the unit-detectors. In addition, alignment verification would be required to guarantee precise data acquisition. These calibration and alignment processes are essential to obtain accurate and reliable muon tomography measurements. By integrating these theoretical and engineering considerations, the detector array can be effectively moved around the object, acquiring data from multiple angles for precise and comprehensive muon tomography scans.

To simulate the rotation of the sub-detector, we replicated the sub-detector by creating four copies on both sides of the original position, forming an arc-like arrangement. This setup models the geometry of the sub-detector's rotation and the paths of muons through the system. In Fig. 6.5 we see the arc on the bottom, and the distances for a block of 250 cm in length.

Finally, Fig. 6.6 illustrates how muons interact with the detector and the target object. As muons traverse the object, their interactions vary: some are absorbed, others are scattered, and some pass through to reach the sub-detector on the opposite side of the target. The simulated rotation of the sub-detector enables the collection of data at multiple angles, improving the measurement of the scattering angle distribution.

To correlate hits in the detectors and reconstruct muon tracks, a time-tagging system would be required in a real experimental setup. However, in our simulations, we do not account for systematic uncertainties arising from reconstruction inefficiencies related to time stamping. Instead, we used Monte Carlo (MC) truth data, specifically the secondary particle identification number for each event, to accurately reconstruct the muon direction based on the energy deposition in the corresponding unit detector.

We used this idealized reconstruction scheme to quantify the angular dispersion induced by multiple Coulomb scattering in different materials and to

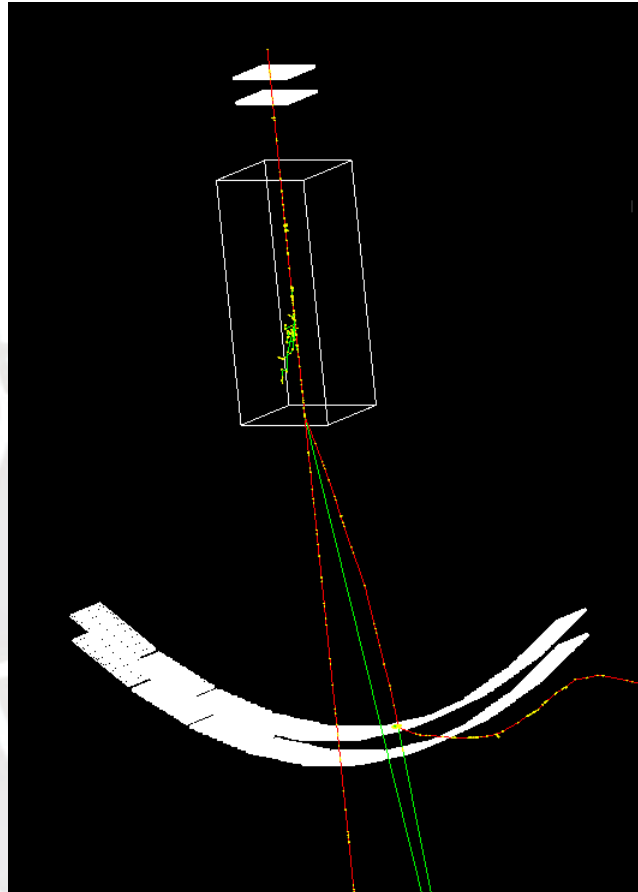


Figure 6.6: GEANT4 simulation setup showing 1 particles coming from a single air shower, with the second sub-detector rotated approximately  $90^\circ$  around the central point. The particle trajectories are color-coded as follows: red lines are negative charged particles (e.g., muons and electrons), green lines correspond to photons, and yellow points indicate physical interactions. The geometry of the sub-detectors and the target object is shown as white lines.

obtain statistically robust results for material discrimination. However, in a realistic experiment, the cosmic muon flux arrives from different directions, and track reconstruction would require additional considerations, such as incorrect associations of spatially and temporally uncorrelated hits or accidental coincidences due to unrelated particles within finite coincidence windows. These effects would enlarge the uncertainty on the angular width of the scattering distributions and, consequently, increase the observation times required to distinguish between materials.

Despite these limitations, the present results provide a reference for defining the minimum detector performance and observation time required for future experimental realizations of muon scattering tomography systems.



# Chapter 7

## Results and Discussion

This chapter presents the results obtained from the simulations carried out in this study. The primary aim of our analysis is to discern between different materials (i.e., water, air, concrete, aluminum, iron, and lead) by applying statistical methods in muon tomography. We quantify and compare the observed variations among the various materials in the simulations. A higher sigma deviation between material parameters will indicate a more reliable differentiation.

As explained in the previous chapter, we used particle showers simulated in CORSIKA for a period of one hour, with the particle traveling in a single direction. Muons arriving at ground level will continue their trajectory deviated, depending on the object's material composition and size.

These muons will first pass through the detector positioned before the object (i.e., the block) and then pass through the block. We tested two methods to find differences between blocks of different materials: (1) using the number of detected particles and (2) using their scattering angles. To calculate these angles and the number of particles detected, we used the tracks, shower ID (the identifier for the showers), event ID (the identifier for individual particles), positions, and momentum directions of the muons from both simulations.

### 7.1. Simulation Setup

The simulation of muon tomography using a scintillator-based detector was conducted to analyze the flux of cosmic rays across a range of energies from  $10^2$  to  $10^6$  GeV. The initial flux was generated using the CORSIKA software package. In Chapter 3, we presented the distributions of muon radii at ground level (Fig. 3.3) and muon energy distributions (Fig. 3.4) for a thousand showers initiated by primary protons at different fixed energies. As the energy of the primary particles increases, a corresponding increase in the number of secondary particles and their radial distributions is observed. However, if we want to get a large number of high-energy particles, we require longer measurement times. Figure 3.6 shows the distributions of radii and energies for

muons, electrons, photons, and other particles, confirming that muons constitute the majority of particles at the ground level and possess energies higher than those of other secondary particles. For this reason, we select the muons as input for the detector simulation in GEANT4.

The GEANT4 toolkit was used to simulate the interactions of cosmic rays with the detector and with the object positioned between the two sub-detectors. In this simulation, described in Chapter 6, we determined that the optimal geometric configuration to achieve a  $1^\circ$  angular resolution is achieved with the following distances:  $d$  (the distance between the two planes of each detector) is 0.2 m,  $D'$  (the distance between the first detector and the object) is 0.6 m and  $D$  (the distance between the last detector and the object under study) is 2.80 m. These distances were kept fixed for all tests. While  $d$  remained constant, the positions  $D$  and  $D'$  were adjusted relative to the object to maintain their specified value for different widths of the object.

We investigated different widths of the object  $W$ , which were 50, 100, 150, 200 and 250 cm, together with different materials. Table 7.1 presents the properties of the materials under study, including the atomic number and atomic weight of those made for single element materials (e.g., aluminum, iron, and lead), and the effective atomic number, for compound materials (e.g., concrete, air, and water). The densities of these materials are provided in Table 4.1. In addition, Figure 7.1 illustrates the experimental setup used to measure muon counts and deflected angles after particles pass through a material block.

Materials	Z	A	$Z_{eff}$	Z/A
Water	10	18	7.5	0.555
Air	7.35	14.72	7.6	0.499
Concrete	50.53	100.53	17	0.503
Al	13	26.98	-	-
Fe	26	55.845	-	-
Pb	82	207.2	-	-

Table 7.1: Properties of analyzed materials: atomic number ( $Z$ ), atomic weight ( $A$ ), effective atomic number ( $Z_{eff}$ ), relation between atomic number and weight ( $Z/A$ ) and density.

## 7.2. Comparative Analysis of Two Muon Tomography Methods for Material Differentiation

We have compared two methods of muon tomography for material differentiation using simulations [93]. These methods were as follows:

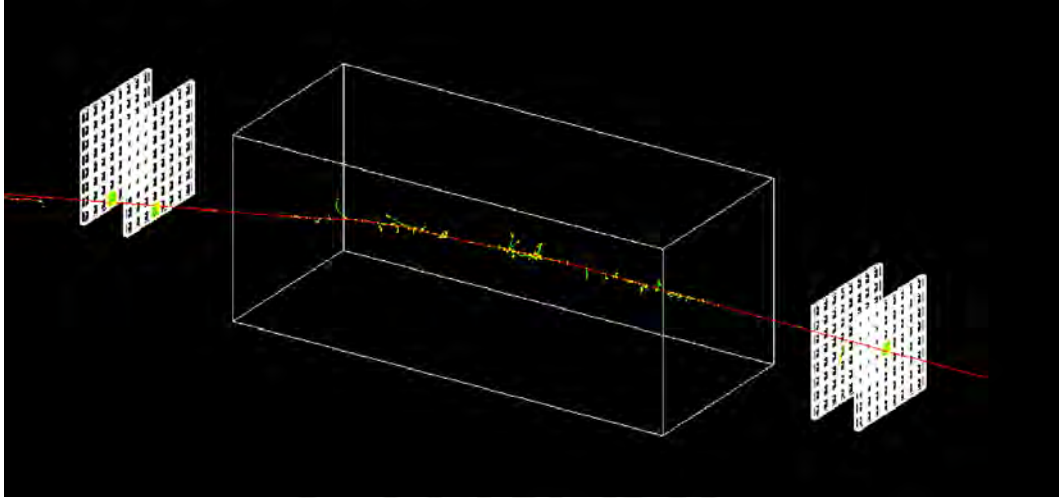


Figure 7.1: GEANT4 simulation of the muon tomographer made of a set of two sensor planes before and two after the analyzed block. The width of the lead block was 2.5 m. A 4 GeV muon event is simulated. Red lines represent negative charged particles (e.g. the muon track and electrons), while the green lines are photons produced by muon interactions in the plastic scintillator and block, and the yellow points represent step points or physical processes.

1. Absorption method: Absorption of particles that arrive at the last detector, comparing the following fractions:
  - 1A) Fraction between the particles that reach the second sub-detector (located after the object) out of the particles that successfully pass through the entire detector system after traversing an air block.
  - 1B) Fraction between the particles that reach the second sub-detector (located after the object) out of the particles that hit the first sub-detector (i.e., the number of particle that should have arrived in the absence of any object)
2. Scattering method: Width of the Gaussian fit of the scattering angle distribution.

By comparing the measured parameters (fraction of detected particles and width of the Gaussian fit), we find the differences between the materials, calculating the number of sigma deviations between them, thus quantifying the differences between materials. We investigated the variations for different materials and block widths.

The number of sigmas is calculated with the following formula:

$$\sigma = \frac{\|x_A - x_B\|}{\sqrt{\text{Err}(x_A)^2 + \text{Err}(x_B)^2}} \quad (7.1)$$

where  $\sigma$  is the number of sigmas,  $x_A$  and  $x_B$  are the variables (i.e., fractions or Gaussian fit width) for each different material (i.e., A and B) and  $\text{Err}(x_A)$  and  $\text{Err}(x_B)$  are their corresponding errors.

### 7.2.1. Absorption method

We present the results of the two variations of the first method (1A and 1B) for material differentiation in muon tomography. The fundamental observable for both methods is a fraction  $x$ , defined as the ratio of particles that arrive at the second sub-detector ( $N_f$ ) to a reference number of particle ( $N_i$ ):  $x = \frac{N_f}{N_i}$ . The two variations of the first method differ in how they define the reference ( $N_i$ ). Figure 7.2 shows the fractions of detected particles for the first variation (Method 1A), where  $N_i$  is defined by the air block as a standard reference because the muons deviate the least when passing through it, resulting in the mean fraction of 1. Figure 7.3 shows the results for the second variation (Method 1B), where  $N_i$  is the initial particle count and the fraction decreases as the block width increase; for air, the mean fraction in this case is 0.93. Both figures show results for several materials as a function of block width.

For both variations, the uncertainty (error) associated with the fraction  $x$  for each material is derived from Poisson statistics ( $\sigma_N = \sqrt{N}$ ) and is given by:

$$\text{Err}_{frac} = \frac{N_f}{N_i} \sqrt{\frac{\sigma_{N_i}^2}{N_i^2} + \frac{\sigma_{N_f}^2}{N_f^2}} = \frac{N_f}{N_i} \sqrt{\frac{1}{N_i} + \frac{1}{N_f}} \quad (7.2)$$

The statistical significance (e.g., the number of sigmas differentiating two materials) is subsequently calculated from the error propagation, assuming that the variables ( $N_{fA}, N_{iA}, N_{fB}, N_{iB}$ ) are independent.

The result displayed in both figures 7.2 and 7.3 shows that materials can be differentiated in most cases, except for aluminum and concrete, whose curves are close. This observed hierarchy of attenuation is directly correlated with the intrinsic properties of the materials. After air, the water block exhibits the next highest fraction of transmitted particles. This is consistent with the fact that water has the second-lowest atomic number (see Table 7.1) and density (see Table 4.1) among the materials studied. The curves for concrete and aluminum show fractions lower than those for water, as they have higher density and atomic number. Finally, iron and lead demonstrate the highest absorption and the lowest fraction, as they possess the highest density and atomic number.

In Fig. 7.4 we show the comparison between the fractions curves for both variations of this method versus the widths of the iron block. Both variations of the first method and its results are very similar. This similarity is calculated with the number of sigmas, which ranges from 1.5 to 2  $\sigma$ s for the different widths of the object.

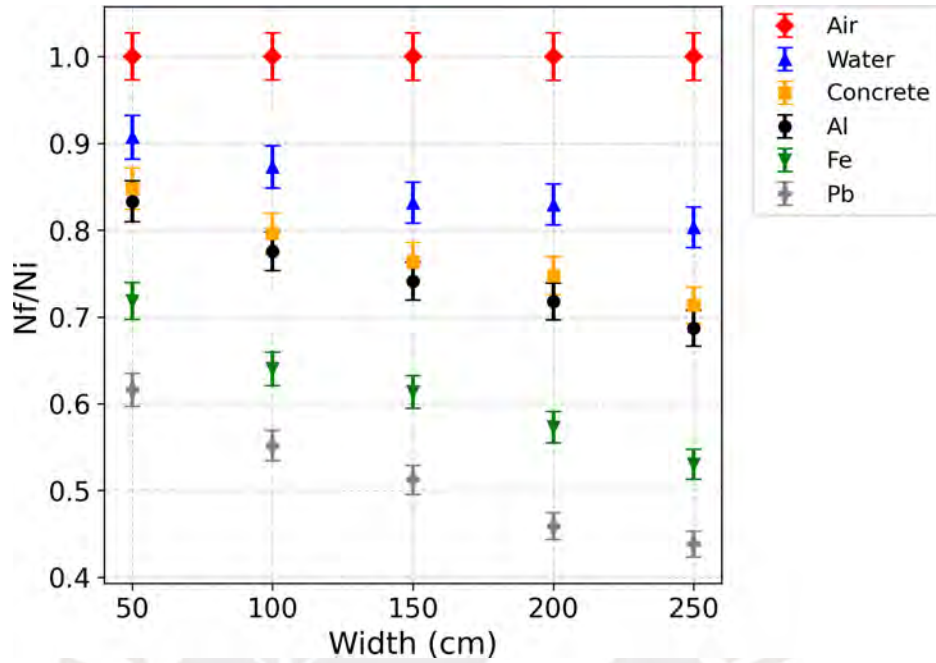


Figure 7.2: Method 1A: Fraction of particle detected in the sub-detector after the object ( $N_f$ ) versus the number of particles that arrive at the same detector after traversing an air block of identical size  $N_{air}$  for different materials as a function of block width.

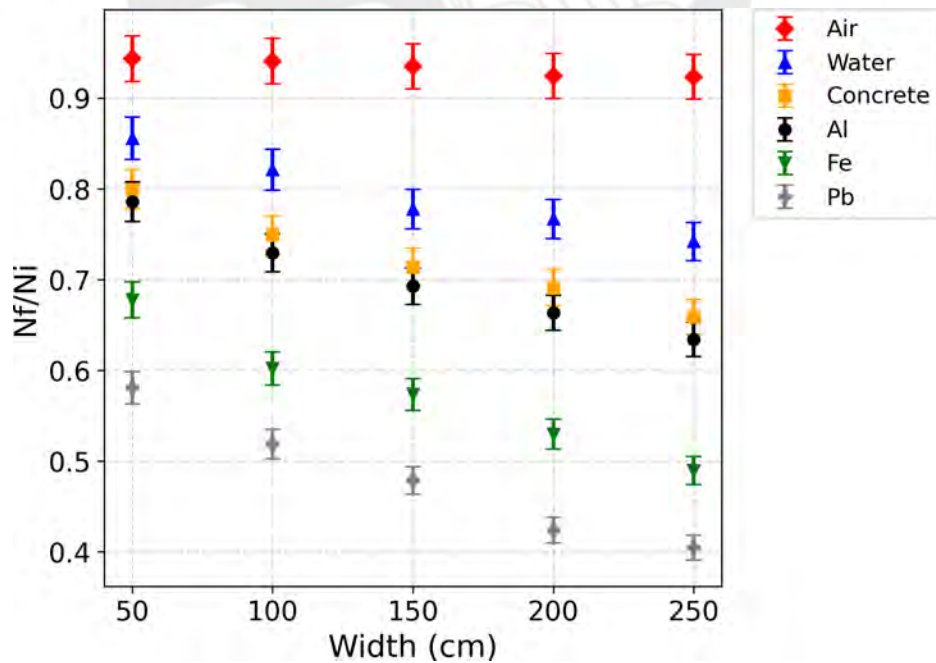


Figure 7.3: Method 1B: Fraction of particle detected in the sub-detector after the object ( $N_f$ ) versus the number of particles detected in the sub-detector before the object ( $N_i$ ), for different materials as a function of block width.

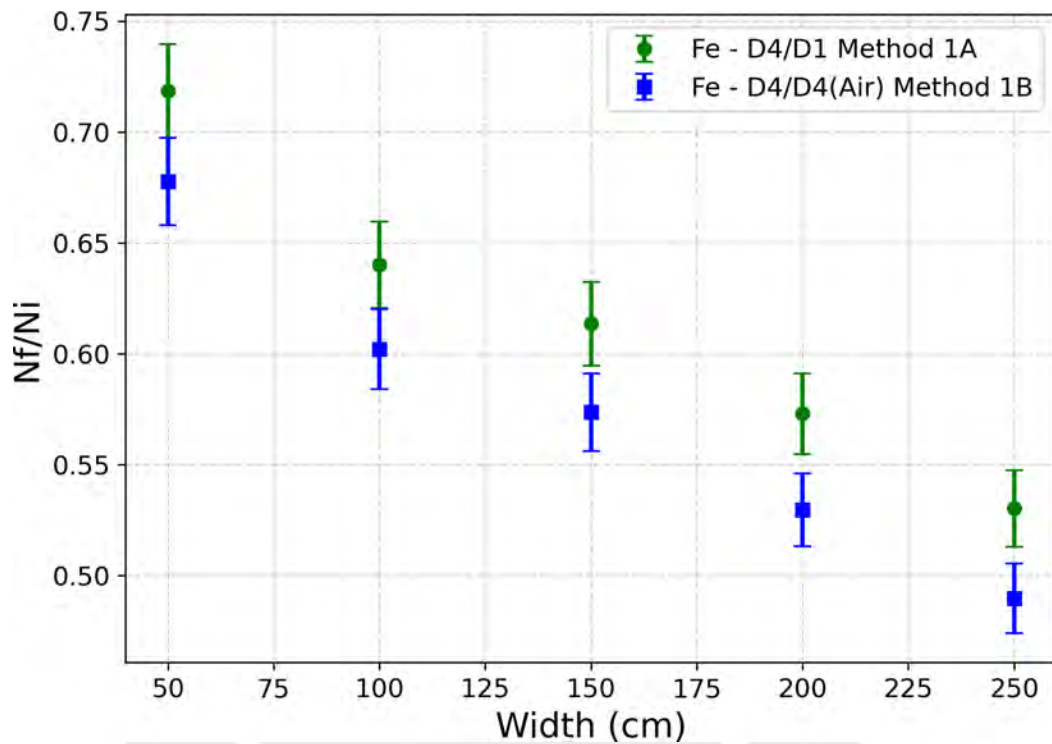


Figure 7.4: Green circle: Method 1A (Fraction between muons detected in last detector for an object made of iron (Fe) and muons detected in the last detector after traversing an air block of the same size) measures attenuation relative to a standard reference material (air) and Blue square: Method 1B (Fraction between muons detected in last detector for the block made of iron (Fe) and muons in the first detector (i.e., without any object in between) measures attenuation relative to the initial beam intensity).

Furthermore, we analyzed the impact of different block widths on the fraction of detected particles. As the width of the block increased, the differences in attenuation between materials became more pronounced. This observation aligns with theoretical expectations and demonstrates the effectiveness of this method in distinguishing materials on the basis of their muon attenuation characteristics.

To quantify the differentiation between materials, we calculated the statistical significance (number of sigma deviation  $\sigma$ ) between the fractions for different materials for the absorption method 1A. Higher sigma values indicate greater confidence in the differentiation of the material. As seen in Fig. 7.6, the sigma differences between lead and iron are approximately  $5\sigma$ . In contrast, the sigma differences between lead and aluminum were much larger, above  $10\sigma$ . This indicates that, in terms of muon attenuation, lead is more similar to iron than aluminum.

Moreover, the results show a relatively small sigma difference of  $1\sigma$  between aluminum and concrete, indicating that their attenuation properties are similar. We observe that our results follow the trend of the effective atomic number (Table 7.1) and density (Table 4.1) of these materials. We compare these results with the theoretical exponential attenuation model taking into account that a more realistic description must include the muon energy spectrum. In this approach, muons follow a power law distribution  $\phi(E) \propto E^{-\gamma}$  with  $\gamma \approx 2.7$ , where  $\phi(E)$  represent the differential flux of muons (the number of muons per unit area, time, solid angle and energy). Only muons with energy above a threshold  $E_{min} \approx \alpha x$  can cross a material thickness  $x$ , where  $\alpha$  is the mean energy loss rate of muons in the material (in unit of MeV/cm). This model naturally predicts a stronger attenuation than the pure exponential law and provides a better agreement with the simulated data as shown in Fig. 7.5. Here  $\alpha$  correspond mainly to the ionization losses in the general expression that we describe in Eq. 4.5 of this work. The typical values of  $\alpha$  [59] justifies the linear approximation  $E_{min} \approx \alpha x$ .

### 7.2.2. Scattering Method: Width of the Gaussian Fit to the Scattering Angle

This method quantifies material interaction by analyzing the Full Width at Half Maximum (FWHM) of the Gaussian fit to the muon scattering angle distribution. The scattering angle is identifying the muon Monte Carlo truth hit positions from the emitted scintillation photons of each sub-detector plane, rather than relying on the geometric center of each pixel. Although these precise hit positions are not directly measurable in practice, this approach simplifies the simulation. The inherent angular resolution error, which remains below  $1^\circ$ , is accommodated by using  $1^\circ$  bins when calculating the angular deviations.

Trajectory vectors are constructed by connecting the hit position across

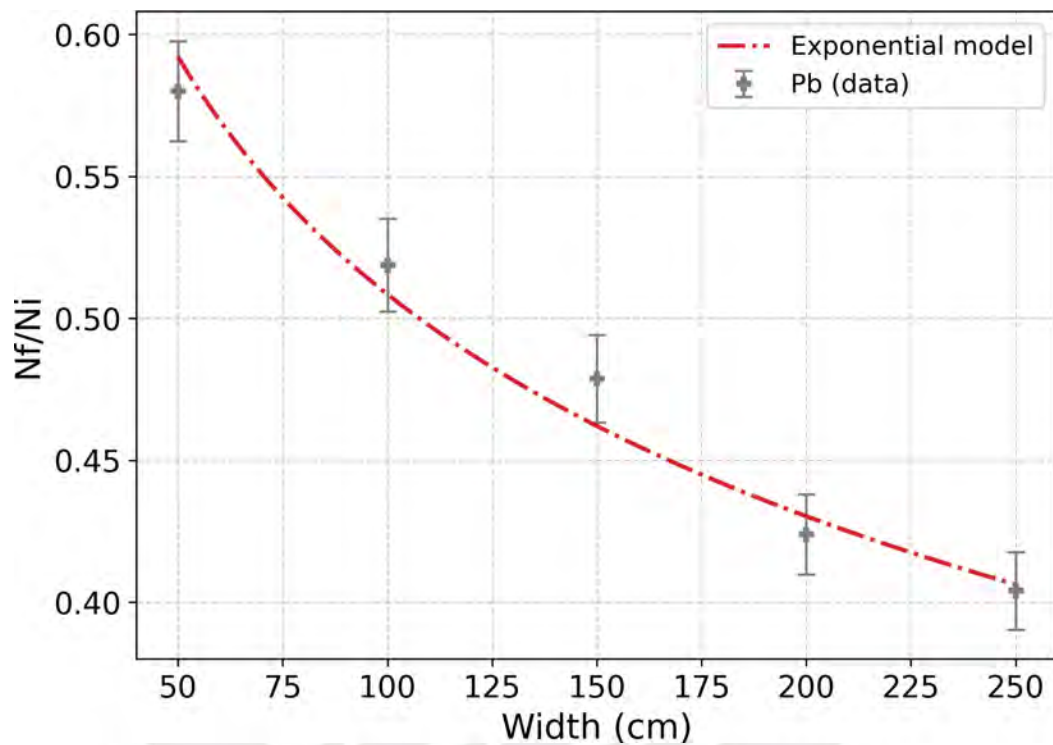


Figure 7.5: Fraction of particles simulated detected in the sub-detectors after the lead object and those that should have arrived to the fourth detector through air block changing with the width of the block compared with the theoretical curve  $F_{\mu}(L) = \exp - \frac{(dE/dx)_{\rho}}{E_0} L$  (model described in [94]) for the same material.

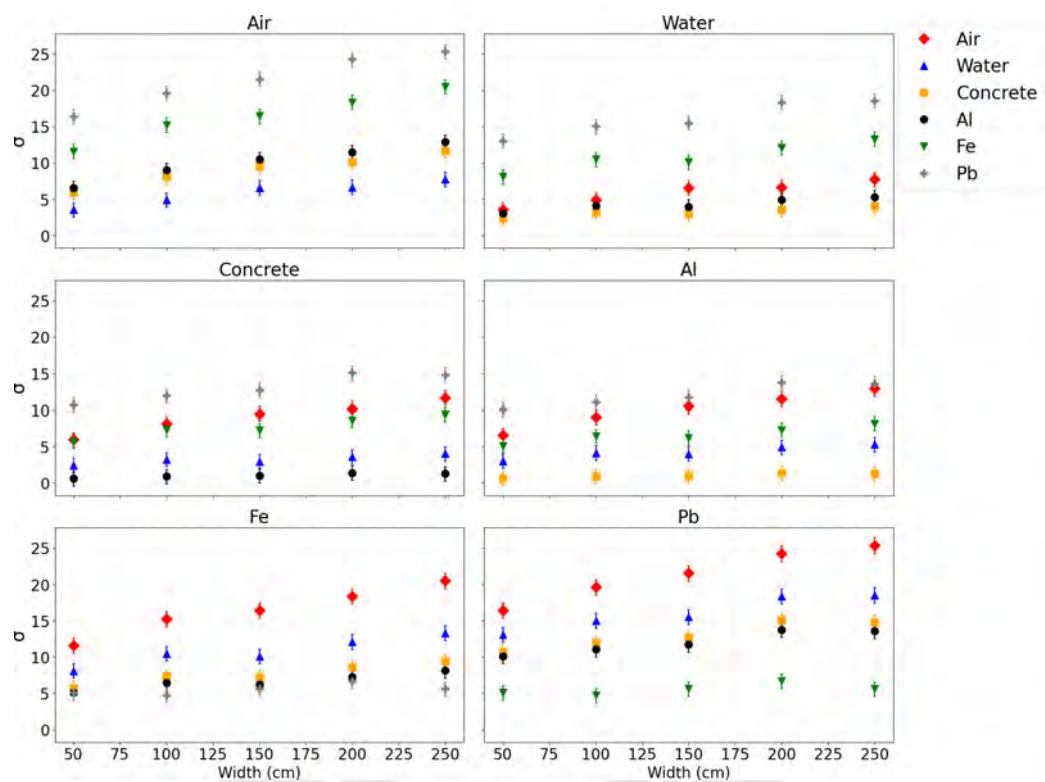


Figure 7.6: Number of sigma deviations between the material stated on top of each plot compared with those in the legend using the absorption method.

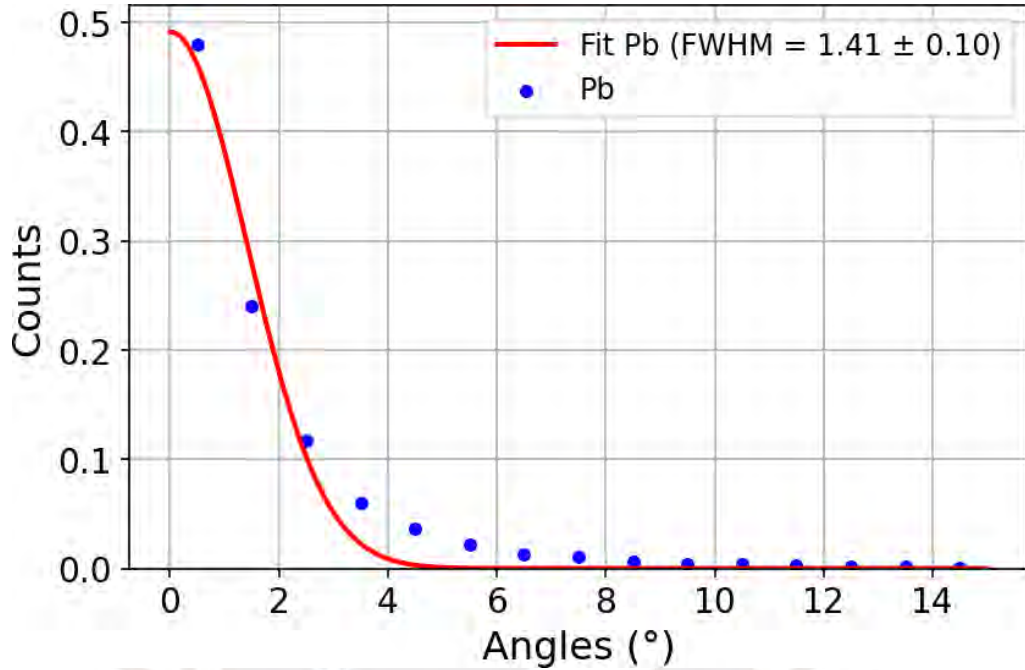


Figure 7.7: Gaussian fit to the scattering angle distribution for a 250 cm block of lead.

sensors within each plane of the sub-detectors. The scattering angle  $\theta$  is determined by comparing the incident vector  $\vec{a}$  (from the sub-detector above the object) and the outgoing vector  $\vec{b}$  (from the sub-detector below the object) using the formula:

$$\theta = \arccos\left(\frac{\vec{a} \cdot \vec{b}}{\|\vec{a}\| \|\vec{b}\|}\right) \quad (7.3)$$

For each material and block width, we constructed a distribution from the deviation angles of all transmitted muons and fitted with half of the Gaussian function because of the positive angles. For example, Figure 7.7 shows the half of the Gaussian fit for the distribution of the scattering angle of a 250 cm wide lead block. The corresponding width of the Gaussian fit is  $1.41^\circ$ .

Our simulation shows that each material exhibits a unique scattering signature, allowing for differentiation based on these properties. This is illustrated in Figure 7.8, where the distribution of lead is wider than that of iron, indicating a greater multiple scattering. In contrast, the distribution for concrete is significantly narrowed compared to those for both lead and iron, resulting in a much smaller dispersion of scattering angles.

To quantify these differences in scattering signatures, the FWHM of each angular distribution was determined through the half of the Gaussian fitting. The uncertainties of these FWHM values were derived from the covariance

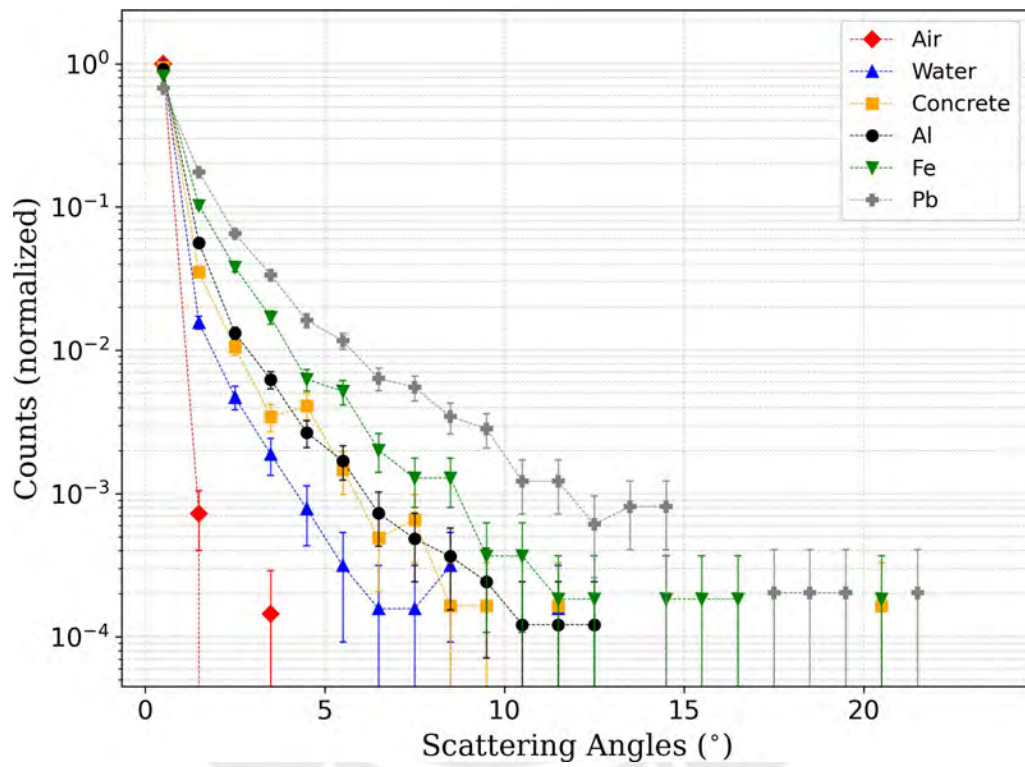


Figure 7.8: Scattering angle distributions for all materials using a 250 cm block. Histograms are normalized.

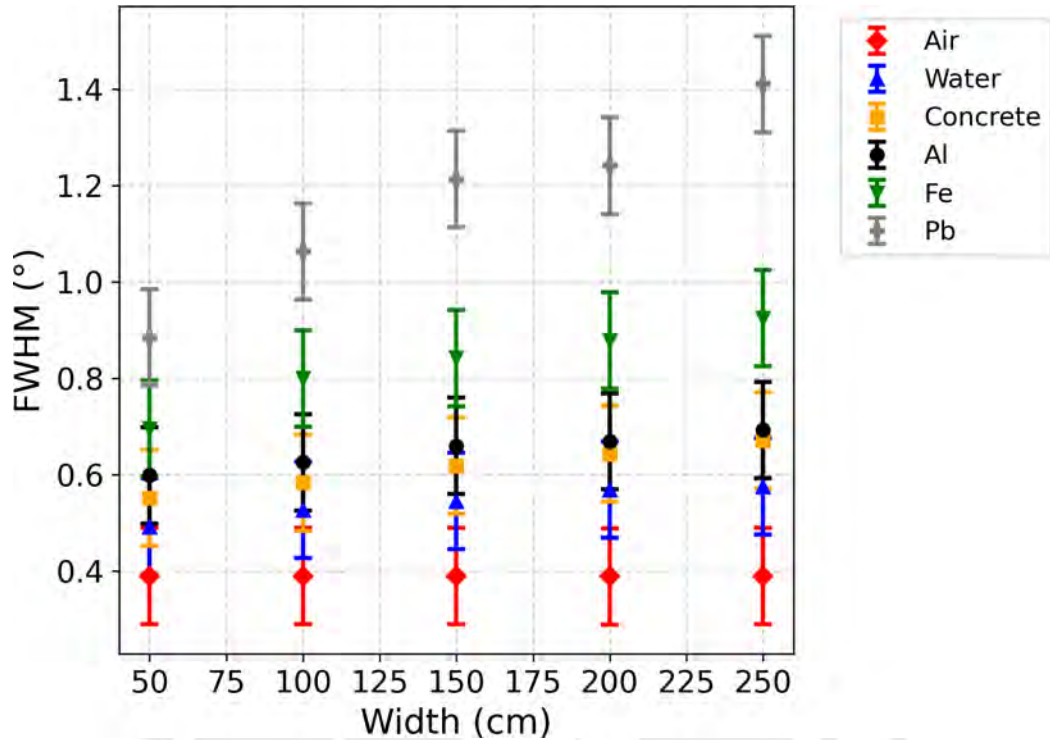


Figure 7.9: Width of the Gaussian fit of the scattering angle distribution varying the width of the block for different materials.

matrix of the fitting algorithm (implemented via `spicy.curve-fit` in python). The statistical uncertainties were then combined in quadrature with a fixed systematic angular uncertainty of 10%, which represents a conservative fraction of the expected detector angular resolution ( $0.1^\circ$ ), to yield the total uncertainty for each measurement. The statistical significance of the difference between any two materials was subsequently computed using standard error propagation techniques, under the assumption of statistical independence.

Similarly to the absorption method, we explored the influence of block width on the FWHM of the Gaussian fit to the scattering angle distribution, revealing a predictable scaling law that enable material discrimination. The results shown in Fig. 7.9, demonstrate that wider blocks resulted in broader scattering angle distributions, indicating increased muon interactions and scattering effects. The FWHM for lead curve is observed to diverge from all other materials as the block width increases, followed by the iron curve. In contrast, the FWHM values for less dense materials like aluminum and concrete, while following the same increasing trend, remain much closer to each other, making difficult to differentiate due to overlapping error bars.

To quantify the differentiation capacity, we calculated the statistical significance (number of sigma) using Eq. 7.1 to compare the width of the Gaussian fit between material pairs. The results of this analysis are shown in Fig. 7.10.

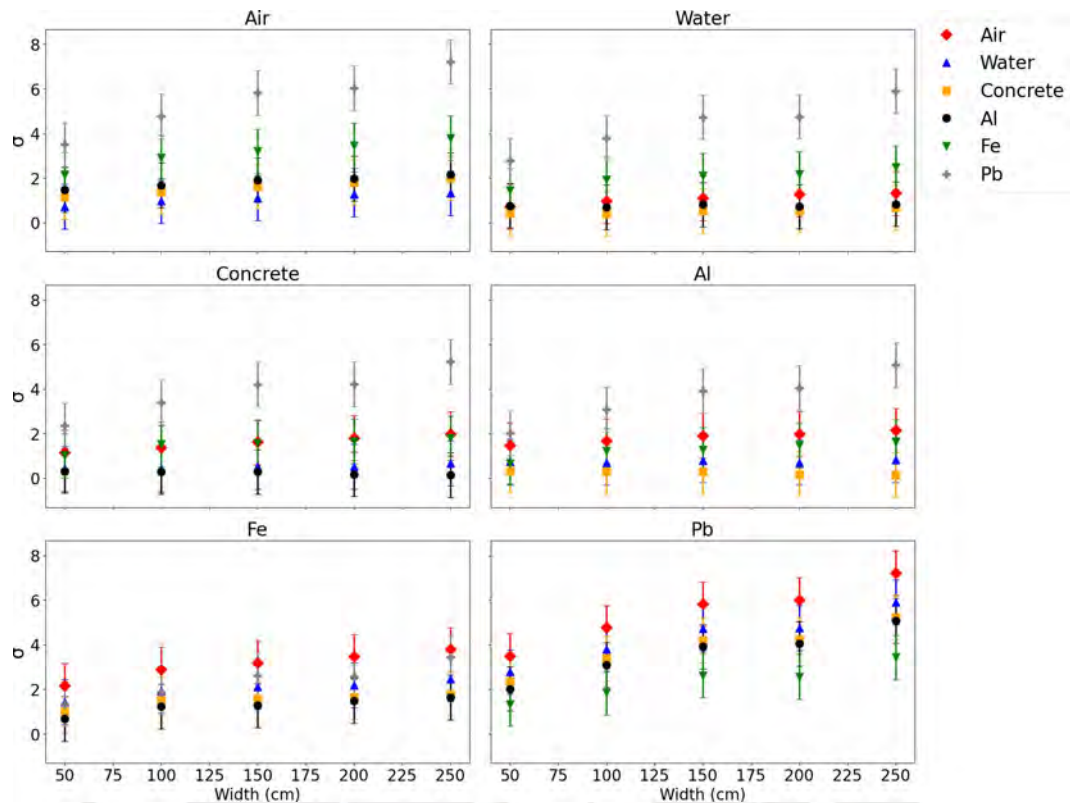


Figure 7.10: Number of sigma deviations between different materials taking into account the Gaussian fit width of their scattering angle distributions.

Similarly to the absorption method, the differences between the materials become more distinct with increasing width of the block. For the smallest size (50 cm), muons pass through with minimal deviation, resulting in lower statistical separation. As the block width increases to 250 cm, the number of sigmas increases significantly for material pairs with differing atomic numbers.

A crucial aspect is that lead, being denser and causing greater muon absorption and scattering, shows a larger statistical separation (higher number of sigmas) from aluminum, concrete, water, and air, as their scattering curves are similar. This indicates that differentiating between these similar materials would be challenging and would require significantly longer observation times to accumulate sufficient statistics.

To validate our simulation, we compare the simulated FWHM as a function of the size of the block with the theoretical curve of Eq. 4.14 in Fig. 7.11. The theoretical prediction is close to the simulated data, with the trend of the theoretical curve, indicating agreement within  $2\sigma$ .

Using both methods and evaluating the statistical significance (sigma differences), we achieved a comprehensive analysis of material differentiation by muon tomography. These findings contribute to our understanding of the different characteristics and properties of materials that contribute to more ac-

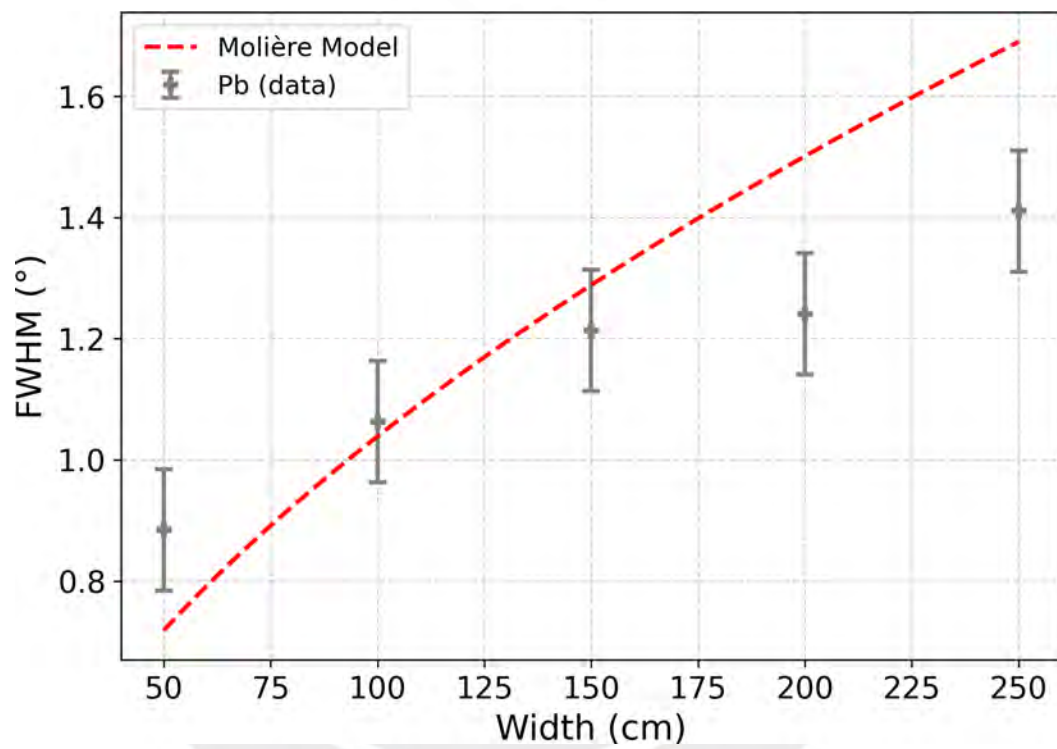


Figure 7.11: Width of the Gaussian fit of the simulated scattering angle distribution for lead changing with the width of the block compared with the theoretical curve based in the Eq. 4.14 for the same material.

curate and reliable material identification in muon tomography applications.

We now compare the two methods used in this study: (1) the fraction of detected particles (absorption) and (2) the width of the Gaussian fit to the scattering angle distribution (scattering).

The first method provides a simple way to differentiate materials, as the results directly represent muon attenuation through different materials. This method offers the advantage of simplicity and ease of interpretation. The second method focuses on the scattering behavior of muons within the material, which classifies materials based on their atomic number and density, consistent with theoretical expectations. The main limitation for both methods is the requirement for sufficient statistics; longer acquisition times are needed to measure enough muons for reliable calculations of both absorption and scattering effects.

To objectively compare these methods, we established a threshold of  $3\sigma$  to indicate statistically significant differences between materials. If the sigma value exceeds this threshold, we can be confident of identifying a material difference.

With the first method (Absorption), it is possible to differentiate between the following materials at the specified block widths with more than  $3\sigma$  confidence from 1.3 days of time of observation:

- Lead and iron can be distinguished from all other materials (air, water, aluminum, and concrete) at any object width.
- Air can be clearly differentiated from concrete and aluminum for all widths.
- Air can be distinguished from water between 100 cm and 250 cm wide.
- Concrete can be differentiated from water for an object between 200 cm and 250 cm wide.

Other comparisons at various widths of the corresponding object cannot be differentiated with more than the  $3\sigma$  threshold. For example, the difference between concrete and aluminum is less than  $1\sigma$  confidence for all object widths, indicating that they are statistically indistinguishable with this method under the current statistics.

With the second method (scattering angle), the following differentiations are possible at specific block widths with more than  $3\sigma$  confidence from 1.3 days of time of observation:

- Lead can be distinguished from iron, aluminum, and concrete for objects 100 cm wide and larger.
- Lead can be distinguished from air and water for all widths above 100 cm.

- Iron can be distinguished from air for objects wider than 100 cm.
- Air can be distinguished from water for objects wider than 100 cm.

Differentiating pairs of other materials requires significantly longer measurement time to achieve a confidence level of  $3\sigma$ .

This work simulated one hour of cosmic-ray showers using CORSIKA, however, to increase the statistics in the GEANT4 simulation, we considered the following:

- The movement of the sub-detector around the object: it would move 4 times to the east and 4 times to the west of the object, effectively multiplying the simulated solid-angle coverage by a factor of 9.
- The initial directions of particles from the cosmic-ray simulation changed to a single direction, while maintaining their initial positions. This increases the number of muons reaching the last sub-detector from 125 to 5423 for the same simulated time, effectively reducing the required measurement time by a factor of 43 approximately

Consequently, the effective simulated time corresponds to approximately 16.4 days of real data acquisition to achieve the sigma levels shown in Fig. 7.6 and in Fig. 7.10. The time required to achieve a confidence level of  $3\sigma$  varies for each pair of materials.

For similar materials, such as aluminum and concrete, the required time is much longer than 16.4 days. For very different materials, such as lead and water, it is significantly less. The specific acquisition times for each case are shown in Fig. 7.12 for the absorption method and in Fig. 7.13 for the scattering method.

In order to compare both methods and the acquisition time, we set a practical threshold of one week to achieve a  $3\sigma$  difference and find:

For the first method (Absorption):

- Between lead and air or water or aluminum or concrete, the acquisition time is less than 1 week for an object of 50 to 250 cm widths.
- Between iron and air or water the acquisition time is less than 1 week for an object of 50 to 250 cm widths.
- Between air and aluminum or concrete the acquisition time is between 3 days and 1 week at all widths of the object.
- For the other comparison between materials at all widths of the object, the acquisition times are more than one week.

For the second method (scattering):

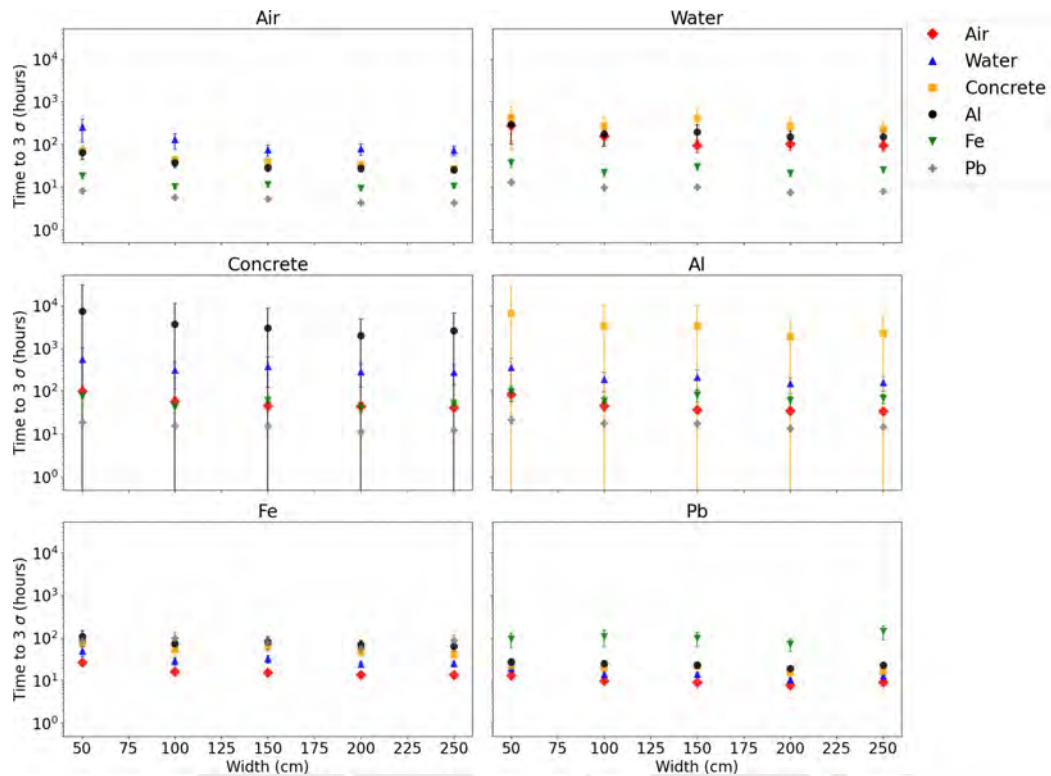


Figure 7.12: Time in hours required to achieve  $3\sigma$  deviation in the fraction of particles detected in the sub-detectors after the object and before it for different object materials.

- Between lead and air, the acquisition time is less than 1 week for an object of 250 cm widths.
- For the other comparison between materials at all widths of the object, the acquisition times are more than one week.

Figure 7.14 shows the sigma values as a function of the object width for a lead block compared to iron. The first method (absorption) consistently yields sigma values higher than those of the second method (scattering). For these reasons, it is more effective for material identification under this condition. However, each method provides complementary information: the first method measures integrated attenuation (sensitive to density and atomic number) and the second method measure the angular extent produced by multiple Coulomb scattering, which is directly measures with radiation length and the microscopic structure of the material. For a comprehensive analysis, both methods can be used together to cross-validate the results and enhance confidence.

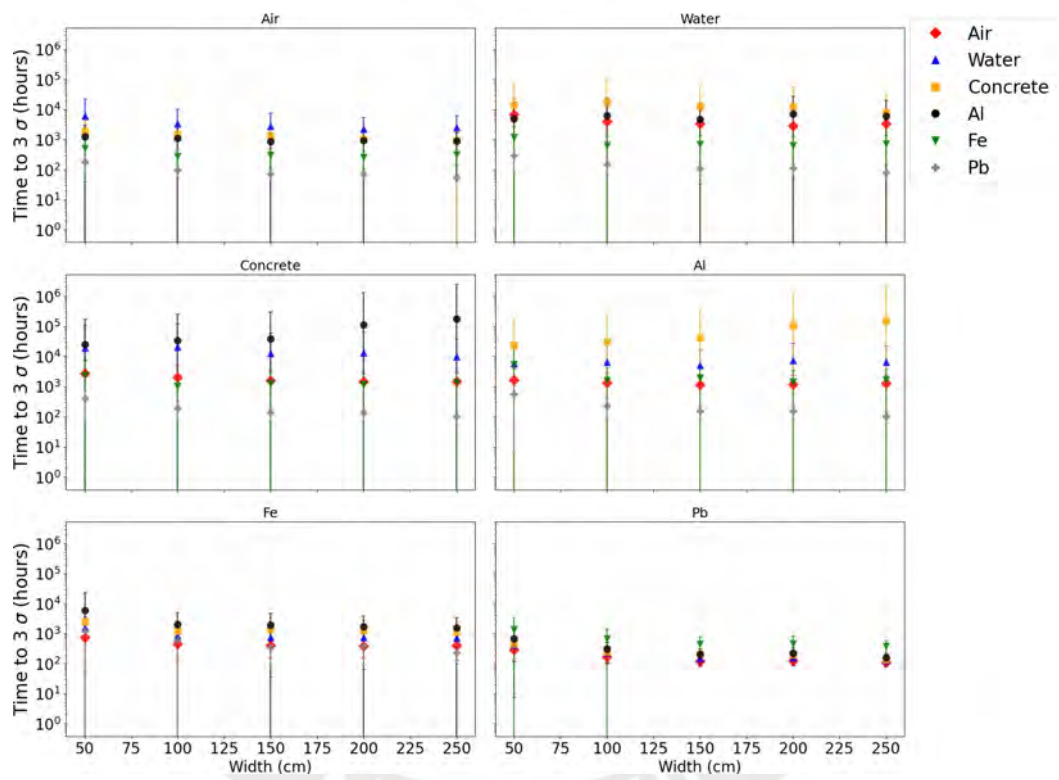


Figure 7.13: Time in hours to achieve 3  $\sigma$  deviation between widths of Gaussian fit of the histograms for scattering angles after passing through the object.

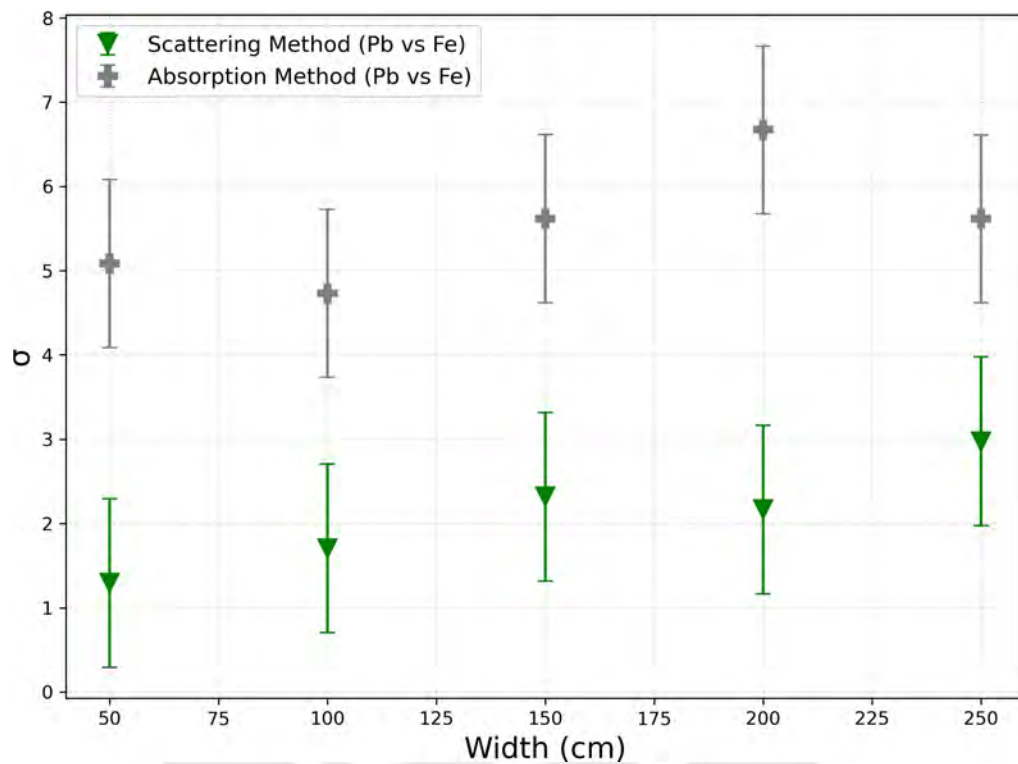


Figure 7.14: Number of sigmas obtained comparing an object made of lead (Pb) and other object made of iron (Fe) showing the two methods studied in this work. Grey points: Absorption Method and green points: Scattering Method.

# Chapter 8

## Conclusions

In this work, we have designed, simulated and analyzed a portable detector for muon tomography, an innovative technique for non-invasive scanning of mid-to large-size objects in fields such as archaeology, geology and material science. The detector is based on an array of plastic scintillators and silicon photomultipliers, offering a practical balance between performance and portability.

The detector consists of two sub-detectors, each comprising two 8 x 8 planes of plastic scintillator units housed in aluminum cases, separated by 20 cm. One sub-detector is placed above the object and another below it to measure muon flux attenuation and scattering angles. The entire system is compact (48.4 x 48.4 x 22 cm<sup>3</sup> per sub-detector) and transportable. To enhance angular coverage and statistics, the lower sub-detector can be rotated around the object, covering in total 90°.

The angular resolution of the system is 1° achieved with a plane separation of 20 cm and the distance of 60 cm (object to first sub-detector) and 250 cm (object to second sub-detector). While gaseous detectors typically offer superior angular resolution, their operational complexity makes them less suitable for field deployment. Our design provides an angular resolution that maintain the same order of magnitude, under idealized simulation conditions, as the angular resolutions reported for other portable systems, such as the MuTe telescope (1.8° - 3.0° approximately).

Using CORSIKA and GEANT4 simulations, we generate a realistic cosmic-ray flux and studied muon interaction with objects of different materials (air, water, concrete, aluminum, iron and lead) and widths (50 cm to 250 cm). Muons were confirmed as the most abundant and energetic particles at ground level, making them ideal for tomography.

We implemented two analysis methods: 1. Absorption method: relies on measuring the fraction of muons attenuated by the object. 2. Scattering method: uses the width of the half of Gaussian fit to the scattering angle distribution. Both method were evaluated using a statistical significance threshold of 3  $\sigma$  for reliable material differentiation.

The absorption method proved highly effective for distinguishing materials. Lead and iron were distinguishable from all other materials across all widths. Air could be differentiated from concrete and aluminum, while concrete and water were separable for widths of 200-250 cm. Differentiation between air and water was achievable for widths of 100-250 cm.

The scattering method was particularly sensitive to high-Z materials. Lead could be distinguished from other materials for widths greater than 100 cm, while iron was distinguishable from air for widths greater than 100 cm. However, differentiation between materials with similar densities (e.g., aluminum and concrete) remained challenging, with significance level below  $1 \sigma$ .

The simplified geometry of uniform blocks represents a limitation, as a real-world objects may feature complex geometries, holes or composite materials, but our results already set a limit on which materials could be identified. Additionally, achieving high statistics significance for materials with similar properties (e.g, aluminum and concrete) requires prolonged observation times.

For example, distinguishing lead from aluminum could take  $1.3 \pm 0.2$  days using the absorption method and  $9.4 \pm 3.7$  days using the scattering method. Differentiating aluminum from concrete would require even longer durations due to their low statistical separation (below  $1 \sigma$ ).

This study successfully demonstrates the feasibility of a portable scintillator-based detector for muon tomography. We have established that the absorption method offers robust material differentiation across a wide range of scenarios, while the scattering method provides complementary insights for high-Z materials. To transition this technology from the laboratory prototype into the real world.

Future work should focus on several key areas. This simulation include optimizing detector hardware, such as granularity by implementing scintillator strips or fibers to reduce costs and improve tracking resolution to mitigate experimental uncertainties. Furthermore, advances data analysis techniques are crucial; future effort should focus on creating advanced reconstruction algorithms, such as Maximum Likelihood or Machine Learning models, to significantly reduce the required observation time from days to hours; and integrating both absorption and scattering data into a unified tomographic inversion framework to enhance 3D density mapping. The refinements are important for expanding the practical horizons of muon tomography into fields such as civil engineering, archaeology, and nuclear safeguards.

# Bibliography

- [1] Pierre Auger Collaboration. The Pierre Auger Cosmic Ray Observatory. *Nuclear Instruments and Methods in Physics Research A*, 768:172–213, 2015.
- [2] K. Hakan et al. Analysis of the cosmic ray effects on Sentinel-1 SAR satellite data. *Aerospace*, 62:8, 2021.
- [3] I. Riadigos et al. Atmospheric temperature effect in secondary cosmic rays observed with a two square meter ground-based detector. *Earth and Space Science*, 2020.
- [4] S. H. Neddermeyer and C. D. Anderson. Note on the nature of cosmic-ray particles. *Comprehensive Analytical Chemistry Physical Review*, 51:884–886, 1937.
- [5] R. Kaise. Muography: Overview and future directions. *Philosophical Transaction of Royal Society A*, 377(20180049), 2019.
- [6] E.P. George and G.S. Shrikantia. Observations of the energy-spectrum of the cosmic radiation below ground. *Nuclear Physics*, 1:54–66, 1956.
- [7] L.W. Alvarez et al. Search for hidden chambers in the pyramids. *Sci. New Series*, 167:832–839, 1965.
- [8] K. Morishima et al. Discovery of a big void in Khufu’s pyramid by observation of cosmic-ray muons. *Nature*, 552 (7685):386–390, 2017.
- [9] IceCube Collaboration. Observation of the cosmic ray shadow of the moon with IceCube. *Physical Review D*, 89(10), 2014.
- [10] J. Peña-Rodríguez et al. Design and Construction of MuTe: a Hybrid Muon Telescope to study Colombian Volcanoes. *JINST*, 15(09):P09006, 2020.
- [11] L. Oláh et al. Muographic observation of density variations in the vicinity of Minami-Dake crater of Sakurajima volcano. *Journal of Disaster Research*, 14:701–712, 2019.

- [12] F. Ambrosino et al. The MU-RAY project: Detector technology and first data from Mt. Vesuvius. *Journal of Instrumentation*, 9(02):C02029–C02029, 2014.
- [13] G. Saracino et al. Applications of muon absorption radiography to the fields of archaeology and civil engineering. *Philosophical Transactions of the Royal Society A: Mathematical, Physical and Engineering Sciences*, 377:2137, 2019.
- [14] W. J. Jo et al. Design of a muon tomography system with a plastic scintillator and wavelength-shifting fiber arrays. *Nucl. Instrum. Meth. A*, 732:2013, 568–572.
- [15] C. L. Morris et al. Horizontal cosmic ray muon radiography for imaging nuclear threats. *Nuclear Instruments and Methods in Physics Research B*, 330:42–46, 2014.
- [16] H. Fujii et al. Investigation of the Unit-1 nuclear reactor of Fukushima Daiichi by cosmic muon radiography. *Progress of Theoretical and Experimental Physics*, 4:043C02, 2020.
- [17] JungHyun Bae et al. Image reconstruction algorithm for momentum dependent muon scattering tomography. *Nuclear Engineering and Technology*, pages 1738–5733, 2023.
- [18] K. Chaiwongkhot et al. 3D cosmic-ray muon tomography using portable muography detector. *Journal of Instrumentation*, 17, 2022.
- [19] Z.Y. Wang et al. Electronics design for a muon imaging system using triangular plastic scintillators with wls fiber readouts. *JINST*, 19(02):P02033, feb 2024.
- [20] R. Bajou et al. High-resolution structural imaging of volcanoes using improved muon tracking. *Geophys. J. Int.*, 235:1138–1149, 2023.
- [21] S. Barnes et al. Cosmic-ray tomography for border security. *Instruments*, 13, 2023.
- [22] Y. Xudong et al. A proposed pku-muon experiment for muon tomography and dark matter search. *Physical Review D*, 110:016017, July 2024.
- [23] M. D. Enrico. Muography applied to archaeology: Search and 3D reconstruction of hidden cavities. *Il Nuovo Cimento*, 43 C:126, 2020.
- [24] V. Tioukov et al. Hidden chamber discovery in the underground hellenistic necropolis of Neapolis by muography. *Sci Rep*, 13:5438, 2023.
- [25] D. Lo Presti et al. Muographic monitoring of the volcano-tectonic evolution of Mount Etna. *Nature, Scientific Reports*, 2020.

- [26] J. A. Rengifo and J. L. Bazo. Design of an atmospheric muon tomographer for material identification based on CORSIKA+ GEANT4 simulations. *Nucl. Instrum. Meth. A*, 1081:170819, 2025.
- [27] E. Aguayo Navarrete and A. Bonneville. A low-cost, portable, ruggedized cosmic muon detector prototype for geological applications. *American Geophysical Union*, 2012.
- [28] D. Heck et al. *CORSIKA: A Monte Carlo Code to Simulate Extensive Air Showers*, volume 6019. Karlsruhe Institute of Technology, 1998.
- [29] S. Agostinelli et al. GEANT4—a simulation toolkit. *Nucl. Instrum. Meth. A*, 506:250–303, 2003.
- [30] C. Grupen. *Astroparticle Physics*. Springer Berlin Heidelberg, New York, 2005.
- [31] T. K. Gaisser and T. Stanev. High-energy cosmic rays. *Nuclear Physics A*, 777:98–110, 2006.
- [32] J. J. Beatty et al. Particle Data Group. *Review of Particle Physics*. *Chinese Physics C.*, 40, 2019.
- [33] Y. S. Utomo. Correlation analysis of solar constant, solar activity and cosmic ray. *Journal of Physics: Conference Series*, 817:012045, 2017.
- [34] J.J. Englemann et al. Charge Composition and Energy Spectra of Cosmic-Ray Nuclei for Elements from Be to Ni. Results from HEAO- 3-C2. *Astronomy and Astrophysics*, 233:96–11, 1990.
- [35] S. Thoudam et al. Cosmic-ray energy spectrum and composition up to the ankle: the case for a second galactic component. *Astronomy and Astrophysics*, 595:A33, 2016.
- [36] D. R. Bergman and J. W. Belz. Cosmic rays: The second knee and beyond. *J. Phys. G*, 34:R359, 2007.
- [37] K. A. Olive et al. Particle Data Group. *Review of Particle Physics*. *Chinese Physics C.*, 38, 2014.
- [38] M. S. Longair. *High Energy Astrophysics*. Cambridge University Press, New York, 2011.
- [39] H. Dehghani et al. Studying depth of shower maximum using variable interaction length. *Astrophysics Space Science*, 362(4):89, 2017.
- [40] D. Heck and T. Pierog. *Extensive Air Shower with CORSIKA: A Guide of Users*, volume Version 6.99x. Karlsruhe Institute of Technology, 2020.

- [41] J. A. Rengifo. Disentangling atmospheric cascades started by gamma rays from cosmic rays with CORSIKA. Master's thesis, Pontificia Universidad Católica del Perú, 2017.
- [42] J.L. Contreras, E. Faleiro, J.M.G. Gómez, R.A. Molina, L. Muñoz, A. Relaño, and J. Retamosa. Principal components analysis of cerenkov photon distributions from extensive air showers applied to gev gamma-proton discrimination. *Astroparticle Physics*, 26(1):50–57, 2006.
- [43] S. J. Saff. *Analysis of Simulation and Reconstruction Methods used by the Pierre Auger Observatory*. PhD thesis, University of Adelaide, 2020.
- [44] R. S. Woolf et al. Measurement of secondary cosmic-ray neutrons near the geomagnetic north pole. *Journal of Environmental Radioactivity*, 198:189–199, 2020.
- [45] J. L. Autran et al. Characterization of atmospheric muons at sea level using a cosmic ray telescope. *Nuclear Instruments and Methods in Physics Research Section A*, 903:77–84, 2018.
- [46] Adams et al. Particle-based imaging techniques. *Comprehensive Analytical Chemistry*, 69:315–337, 2015.
- [47] S. Cecchini et al. Atmospheric muons: experimental aspects. *Geoscientific Instrumentation, Methods and Data Systems*, 1, 2012.
- [48] NOAA. National centers for environmental information of NOAA, 2020. <https://www.ngdc.noaa.gov/> Accessed: 2020-06-10.
- [49] S. N. Axani et al. The CosmicWatch Desktop Muon Detector: a self-contained, pocket sized particle detector. *JINST*, 13(03):P03019, 2018.
- [50] H. Asorey. The LAGO CrkTools suite, 2019. <https://github.com/lagoproject/arti> Accessed: 2020-08-10.
- [51] Cutoff rigidity calculator, 2021. <https://crnslab.org/util/rigidity.php> Accessed: 2021-11-03.
- [52] Meuer et al. Muon production in extensive air showers and its relation to hadronic interactions. *Czech J Phys*, 56:A211–A219, 2006.
- [53] P. R. Blake and W. F. Nash. Muons in extensive air showers: I. the lateral distribution of muons. *J. Phys. G: Nucl. Part. Phys.*, 21:129–143, 1995.
- [54] H. Schoorlemmer et al. Characteristics of extensive air showers around the energy threshold for ground-particle-based  $\gamma$ -ray observatories. *European Physical Journal*, 79:427, 2019.

- [55] Haresh Gadey et al. Monte carlo characterization of the cosmic ray muon flux in shallow subsurface geological repositories intended for disposal of radioactive materials. *Applied Radiation and Isotopes*, 166:109209, 2020.
- [56] L. Bonechi et al. Atmospheric muons as an imaging tool. *Reviews in Physics*, 5, 2020.
- [57] P. Shukla et al. Energy and angular distributions of atmospheric muons at the earth. *International Journal of Modern Physics A*, 33:30, 2018.
- [58] G. Galgóczi et al. Imaging by Muons and their Induced Secondary Particles—A Novel Technique. *JINST*, 15(06):C06014, 2020.
- [59] D. E. Groom, N. V. Mokhov, and S. I. Striganov. Muon stopping power and range tables 10 mev–100 tev. *Atomic Data and Nuclear Data Tables*, 76(2):183–356, 2001. LBNL-44742.
- [60] A. Amato. Lecture PHY 432: Physics with muons: From atomic physics to solid state physics - university of zürich, June 2018.
- [61] C. Filosa. *Tomographie Muonique : Du Développement de Détecteurs à la Résolution du Problème Inverse*. PhD thesis, Université Paris Saclay, 2019.
- [62] G. Battistoni for the MACRO Collaboration. Study of photonuclear interaction of muons in rock with the MACRO experiment. *Vulcano Workshop 1998: Frontier Objects in Astrophysics and Particle Physics, Proceedings of the conference*, page 419, 1999.
- [63] O. Catalano et al. Volcanoes muon imaging using Cherenkov telescopes. *Nuclear Instruments and Methods in Physics Research A*, 807:5–12, 2016.
- [64] P. La Rocca et al. Cosmic ray muons as penetrating probes to explore the world around us. *Cosmic Rays*, Zbigniew Szadkowski, IntechOpen, 2018.
- [65] H. F. Schreiner. *Methods and Simulations of Muon Tomography and Reconstruction*. PhD thesis, University of Texas at Austin, 2016.
- [66] E. Rutherford. The scattering of  $\alpha$  and  $\beta$  particles by matter and the structure of the atom”. *Philosophical Magazine*, 21(125):669–688, 1911.
- [67] G. R. Lynch et al. Approximations to multiple Coulomb scattering. *Nuclear Instruments and Methods in Physics Research Section B: Beam Interactions with Materials and Atoms*, 58:6–10, 1991.
- [68] S. N. Axani et al. The desktop muon detector: A simple, physics-motivated machine- and electronics-shop project for university students. *American Journal of Physics*, 85:948–958, 2017.

- [69] X. Li et al. Measurement of the energy of fast neutrons in the presence of gamma rays using a NaI(Tl) and a plastic scintillator. *Nuclear Inst. and Methods in Physics Research, A*, 976, 2020.
- [70] Luxium Solutions. Identification of the substance/mixture and of the company/undertaking, 2025. <https://luxiumsolutions.com/> Accessed: 2025-20-08.
- [71] S. N. Axani. The Physics Behind the CosmicWatch Desktop Muon Detectors. Master's thesis, MIT, 2019.
- [72] A. Pla-Dalmau et al. Extruded plastic scintillator for MINERvA. *IEEE Nuclear Science Symposium Conference Record*, 2005.
- [73] T. Ogawa et al. Analysis of scintillation light intensity by microscopic radiation transport calculation and Förster quenching model. *PLOS ONE*, 2018.
- [74] X. Li. Design and characterization of a plastic scintillation detector system for beta tagging. Master's thesis, University of Jyväskylä, 2019.
- [75] S. Gundacker and A. Heering. The silicon-photomultiplier: Fundamentals and applications of a modern solid-state photon detector. *Physics in Medicine and Biology*, 2020.
- [76] C. H. Chenming. *Modern Semiconductor Devices for Integrated Circuits*, volume Chapter 1. UC Berkeley, 2010.
- [77] B. Banino. How scientists are using cosmic radiation to peek inside the pyramids. <https://www.sciencefocus.com/future-technology/how-scientists-are-using-cosmic-radiation-to-peek-inside-the-pyramids> Accessed: 21.01.2024.
- [78] M. Vanadia for the ATLAS Muon collaboration. Study of the performance of the micromegas chambers for the ATLAS muon spectrometer upgrade. *IEEE Transactions on Nuclear Science*, 64:2, 2017.
- [79] S. Bouteille et al. A Micromegas-based telescope for muon tomography: The WatTo experiment. *Nuclear Instruments and Methods in Physics Research A*, 834:223–228, 2016.
- [80] D. Varga et al. Cosmic muon detector using proportional chambers. *European Journal of Physics*, 36(6), 2015.
- [81] M. J. Delgado González and H. F. Castro Serrato. Construction and characterization of a multiwire proportional chamber detector. *Ciencia en Desarrollo*, 10:2, 2019.

- [82] D. Varga et al. Cosmic Muon Detector Using Proportional Chambers. *European Journal of Physics*, 36(6):065006, 2015.
- [83] G. Mauri. *Development and Characterization of Detectors for Large Area Application in Neutron Scattering and Small area Application in Neutron Reflectometry*. PhD thesis, University Degli Studi di Perugia, 2019.
- [84] G. Aielli et al. Particle detectors at accelerators. *Particle Data Group*, 2019.
- [85] S. Wuyckens et al. A Portable Muon Telescope Based on Small and Gas-tight Resistive Plate Chambers. *Phil. Trans. Roy. Soc. Lond. A*, 377:0139, 2019.
- [86] L. V. Grasso. Designs for muon tomography station prototypes using GEM detectors. Master's thesis, Florida Institute of Technology, 2012.
- [87] X Zhou et al. Applications and Prospects of Muography in Strategic Deposits. *Minerals*, 15:945, 2025.
- [88] D. Poulson et al. Cosmic ray muon computed tomography of spent nuclear fuel in dry storage casks. *Nucl. Instrum. Meth. A*, 842:48–53, 2017.
- [89] L. Schultz et al. *Cosmic ray muon radiography*. PhD thesis, Portland State University, USA., 2003.
- [90] A. Clarkson et al. The design and performance of a scintillating-fibre tracker for the cosmic-ray muon tomography of legacy nuclear waste containers. *Nucl. Instrum. Meth. A*, 745:138–149, 2014.
- [91] H. Gomez. Muon tomography using micromegas detectors: From archaeology to nuclear safety applications. *Nucl. Instrum. Meth. A*, 936:14,17, 2019.
- [92] Luxium Solutions. Bc-400, bc-404, bc-408, bc-412, bc-416, 2025. <https://luxiumsolutions.com/radiation-detection-scintillators/plastic-scintillators/bc400-bc404-bc408-bc412-bc416> Accessed: 2025-23-11.
- [93] J. A. Rengifo. Git-hub-codes-thesis. <https://github.com/jrengifog/Methods-Muography>.
- [94] T. K. Gaisser. *Cosmic Rays and Particle Physics*. Cambridge University Press, 1990.
- [95] A. Zyla et al. Particle Data Group. *Prog. Theor. Exp. Phys.*, 083C01, 2020.

- [96] J. A. Bellido for the Pierre Auger Collaboration. Studies of cosmic ray composition and air shower structure with the Pierre Auger Observatory. *Proceedings of 31st International Cosmic Ray Conference*, 2009.
- [97] H. Tanaka et al. Development of the cosmic-ray muon detection system for probing internal-structure of a volcano. *Hyperfine Interactions*, 138:521–526, 2001.
- [98] M. Corbetta et al. Triple-GEM detectors operation under gas recirculation in high-rate radiation environment. *Nuclear Instruments and Methods in Physics Research Section A: Accelerators, Spectrometers, Detectors and Associated Equipment*, 984:164627, 2020.
- [99] Geant4 Collaboration. *Book For Application Developers*, volume Release 10.6. Geant4 web page, 2020.
- [100] M. Hohlmann et al. GEANT4 simulation of a cosmic ray muon tomography system with micropattern gas detectors for the detection of high Z materials. *IEEE Transactions on Nuclear Science*, 56(3):1356–1363, 2009.
- [101] J. Masias et al. Using a portable muon detector for radioactive source measurements and identification. *Nuclear Instruments and Methods in Physics Research A*, 2019.
- [102] R. R. S. Mendonça et al. Analysis of cosmic rays’ atmospheric effects and their relationships to cutoff rigidity and zenith angle using global muon detector network data. *Journal of Geophysical Research: Space Physics*, 124:9791–9813, 2019.
- [103] D. E. Groom and S. R. Klein. Passage of particles through matter. *Particle Data Group*, 2019.
- [104] J. Poirier et al. Distributions of secondary muons at sea level from cosmic gamma rays below 10 TeV. *Astroparticle Physics*, 17(4):441–458, 2002.
- [105] N. I. Rasha et al. Determination of muon absorption coefficients in heavy metal elements. *Journal of Radiation Research and Applied Sciences*, 12(1):281–288, 2019.

# Appendix A

## Flux of Primary Cosmic Rays

We use a file from the LAGO library [50] to calculate the flux of primary CRs, which is modeled as a power law:

$$J(E) = j_0 \times E^{-\gamma} \quad (\text{A.1})$$

The file contain these values: Corsika ID (type of particles),  $j_0$  (constant relate with the number of particles, time, angular distribution and area) and  $\gamma$  (spectral index) for each nuclei from primary CRs. The values are the following:

Nuclei	ID	$\gamma$	Number of showers
H	14	2.77	43307
He	402	2.64	21644
O	1608	2.68	5059
C	1206	2.66	3302
Mg	2412	2.64	1272
Si	2814	2.75	1116
Ne	2010	2.64	985
N	1407	2.72	811
Fe	5626	2.60	777
Li	703	2.54	530
B	1105	2.95	63
S	3216	2.55	208
Be	904	2.75	173
Al	2713	2.66	164
Na	2311	2.66	142
Ca	4020	2.70	106
F	1909	2.69	91
Cr	5224	2.67	71
Ar	4018	2.64	68
Ti	4822	2.61	65
Mn	5525	2.46	59
K	3919	2.65	41
V	5123	2.63	35
P	3115	2.69	32
Cl	3517	2.68	28
Sc	4521	2.64	20

Table A.1: Parameters to calculate the CRs flux reaching the atmosphere and the number of showers generated for 60 min in 0.5 m<sup>2</sup>.